INTERNAL REPORT #53

R. A. Mewaldt

March 12, 1975

CALIBRATIONS OF THE ELECTRON RESPONSE OF THE IMP-H EIS

INTERNAL REPORT NO. 53

Calibrations of the Electron Response of the IMP-H EIS

TABLE OF CONTENTS

I. INTRODUCTION

Measurements of electrons near ~ 1 MeV are complicated by the large amount of scattering that occurs at these low energies (Lupton and Stone, 1972a, 1972b; Internal Report # 28), and by background due to Compton scattered electrons (Hurford et. al., 1974). For this reason laboratory calibrations are imperative to an understanding of the response of a low energy electron detector. This internal report summarizes calibrations of the low-energy electron response of the Caltech Electron/Isotope Spectrometer on IMP-H (IMP-7). Pre-launch calibrations of the flight instrument were performed using monoenergetic electron beams (0.1-3 MeV) from the SRL β-spectrometer. Similar calibrations have been carried out on the initial detector configuration of the IMP-J instrument.

Included in this report are summaries of the experimental setup, data analysis procedures, interpretations of the results and examples of flight electron spectra. Particular attention is paid to various problems with the β-spectrometer and EIS instrument that arose during the course of these calibrations, since they often affect interpretation of the data. Recommendations for future calibration of this type are also included.

Analysis of the EIS electron response to date has concentrated on the wide geometry mode. Further analysis of the calibration data is planned in the course of investigation of various studies of flight electron data, and will be included as Addenda to this report.

Figure I-1 shows the IMP-H EIS detector stack. This report will assume a general familiarity with the operation of the instrument and the nature of the information available from it.

FIGURE I-1

CALTECH ELECTRON/ISOTOPE SPECTROMETER

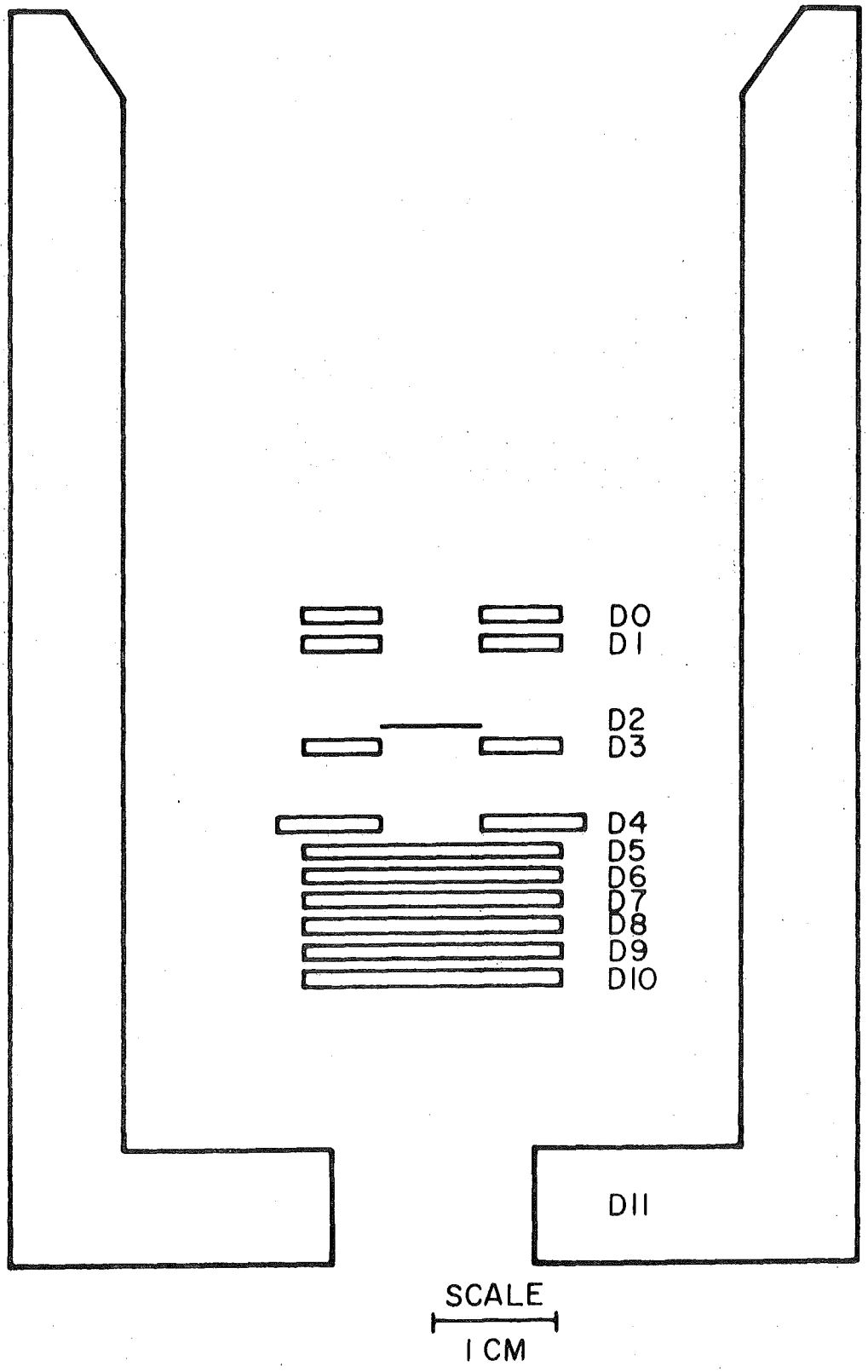

II. EXPERIMENTAL SETUP

A. General Information

Fig. II-1 diagrams the experimental setup used in the β-Spectrometer calibrations. The instrument was mounted in a rotatable support ~ 3' above the beam exit slits. A large bell jar enclosed the instrument and provided the vacuum environment necessary for the electron beam. An externally operable worm-year arrangement allowed the instrument to be rotated with respect to the beam through the angular range $+15^{o} \leq \theta \leq -45^{o}$. The internal Ru^{106} source provided monoenergetic electron beams over the range $.1 \lesssim E \lesssim 3.2$ MeV. The electronic output of the EIS was carried to the GSE through a vacuum feed-through connector mounted in the β-Spectrometer baseplate. Data was recorded on mag-tape using the Varian 520i program BTP2 (Curt Widdoes) in the standard fashion.

Information on the operation of the β-Spectrometer can be otained from the β-Spectrometer Manual and Internal Reports # 28 and # 34. This report will emphasize only those aspects of the spectrometer affecting interpretation of the EIS calibration data.

Various details of the experimental setup differed from one calibration period to another. Table # II-1 summarizes these variations, and other experimental considerations.

Modifications to the β-Spectrometer setup required for these calibrations were performed by Sol Vidor. Details of the experimental setup can be obtained from his notebooks. Stu Hartman was responsible for many of the modifications prior to the IMP-J stack calibrations.

Table II-1 Experimental Details of IMP-H β-Spectrometer Calibrations

Dates (1972)	Rotation Axis	Corrected Angular Range	D5 Unstim. ch #	Experimental Problems	Instrument Problems	GSE Problems
1/31-2/1	Front of D11 Opening	$+20^{\circ}$ to -32°	0.3			Low Statistics for Rates
2/26-2/28	DØ	$+12.5^{\circ}$ to -35°	4.3		D3 Noise	
3/6-3/8	DØ	$+16^{\circ}$ to -5°	4.0			No Pen Rate
3/9-3/10	DØ	$+10^{\circ}$ to -44°	3.9	Th^{228} Source Background	D1 Off	Noisy Rates No Pen Rate
4/25-4/26	DØ	$+12.5$ to -44°	4.1*		D3,D8 Noise	

*Unstable at times

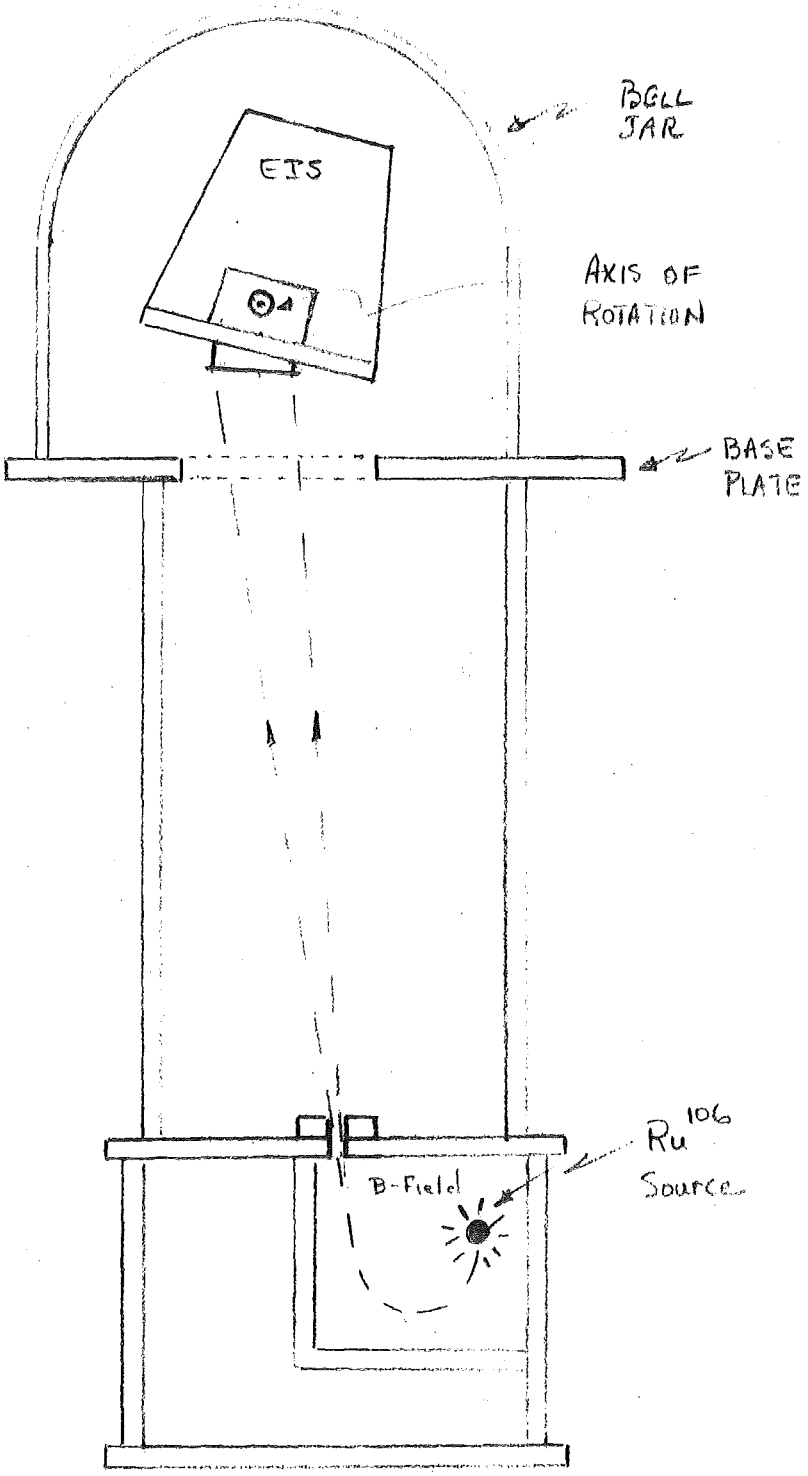

FIGURE II - 1 Schematic Diagram of Beta Spectrometer Setup
Rotatable support for EIS not shown

II.

B. Calibration of the Beta Spectrometer

Extensive measurements of the characteristics of the β-Spectrometer electron beam were performed before and after the actual EIS calibrations. The results of these beam calibrations, along with the various problems that arose, are summarized in this section.

B-1 Energy Calibration

The β-Spectrometer magnet was calibrated by measuring the beam energy as a function of Gaussmeter reading. A 4 mm lithium drifted silicon detector (# 655) was placed at the position that DO occupies when the EIS was mounted in the Spectrometer. Pulse height spectra were taken at ~ 25 magnet settings spanning the Ru^{106} spectrum. The resulting total energy peaks were fit with Gaussians to determine the mean channel number and resolution. The absolute energy of each peak was determined using the pulsar calibration scheme described in SRL IR # 31. Measurements of monoenergetic electrons (Bi^{207}) and alpha particles (Am^{241}) showed a pulse-height defect of 1.8% for electrons in detector # 655 (S. Vidor). This was corrected for in deriving the beam energies.

The magnet calibration used to normalize all data in this report was performed on 5/14/72. Figure II-2 shows a plot of the measured beam momentum $Pc = [E^2 + 2M_e E]^{1/2}$ vs. Gaussmeter reading ($\propto$ B). The excellent linearity allows accurate interpolation for intermediate settings. The conditions of the 5/14/72 calibration were controlled to correspond as closely as possible to those during the EIS calibrations.

II. B-1

Comparison of the 5/14/72 calibration with one performed on 9/19/71 shows a systematic drift of $\sim$ 5-7% in P. For identical Gaussmeter readings, the beam momentum was higher on 5/14/72. The origin of and corrections for this shift are discussed in a later section.

The beam resolution was found to be $\Delta P/P \sim .03 \pm .01$ (fwhm), which is smaller than the EIS channel resolution in most cases of interest.

FIGURE II-2

BETA SPECTROMETER

MAGNET CALIBRATION

(5/14/72)

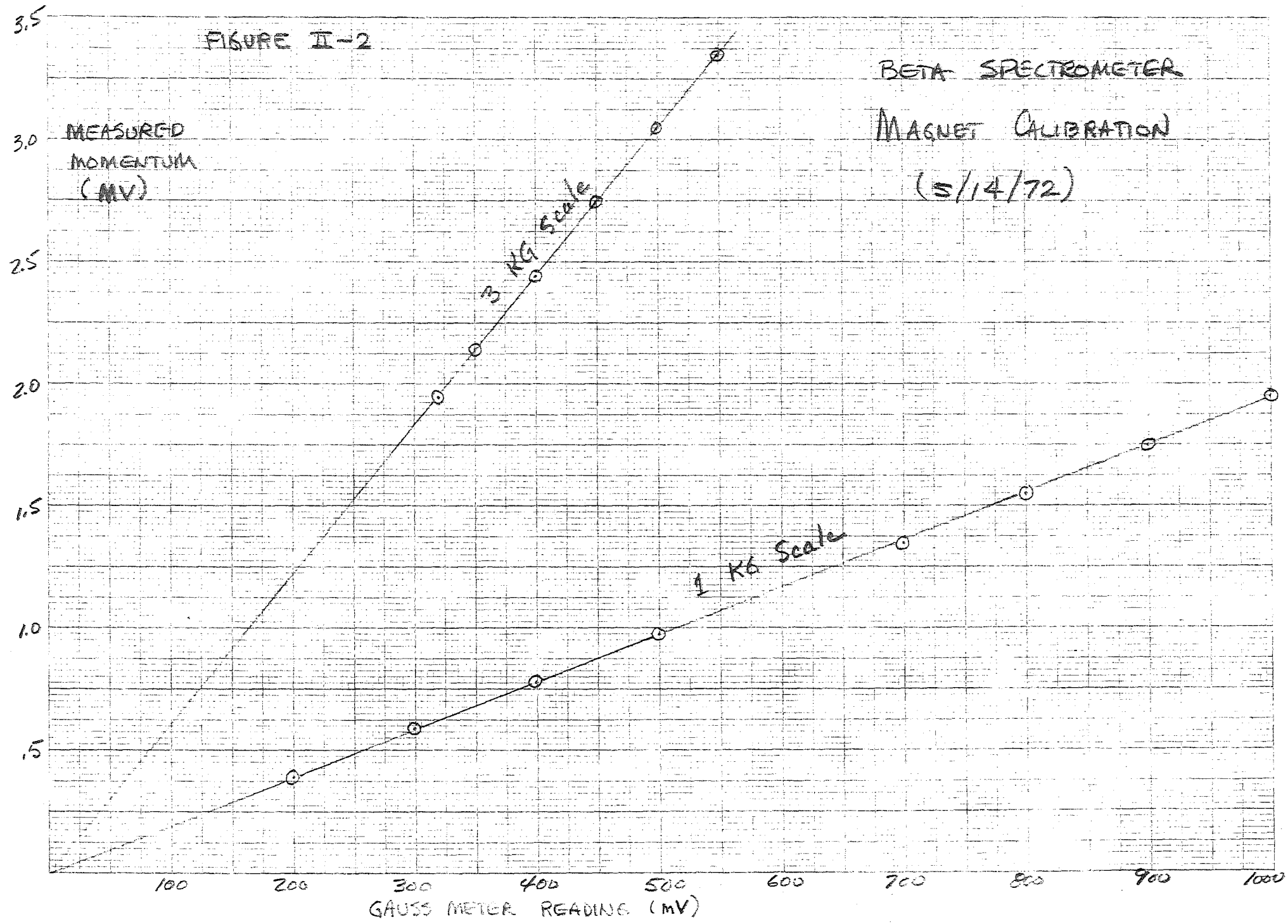

II.

B-2 Intensity vs. Energy Calibration

Knowledge of the absolute intensity of the beam as a function of energy (I(E) in electrons/cm^2·sec) is required to calculate the EIS electron detection efficiencies. The I(E) calibration used in this analysis was performed on 5/13/72. A plastic scintillator counter viewed by a PM tube was used to measure the electron count rate vs. energy. The choice of plastic scintillator (instead of silicon solid state detectors) for this measurement was designed to reduce electron backscattering. An elaborate multistage collimator was designed to further minimize electron scattering effects. The final collimator opening (.755" diameter) was positioned at the location occupied by DO in the EIS calibrations. The collimator opening angle was rotated (using the EIS cradle) to maximize the intensity, and thereby measure the beam angle.

Pulse height spectra were accumulated at all energies used in the EIS calibration. Background spectra (magnet off) were taken periodically to correct the electron spectra for cosmic ray and γ-ray contributions (important only below $\sim$ .5 MeV). The background corrected spectra were integrated to obtain the absolute intensity of electrons in the total energy peak ($\pm 4\sigma$), and the intensity $\geq$ .16 MeV for each beam energy. This data is summarized in Table II-2 and Figure # II-3. The intensity of the total energy peak was used in all determinations of the EIS efficiency. Note from Table II-2 that this may mean that the calculated DO* efficiency at 3 MeV for example, is overestimated by $\sim$ 6%, if a portion of the DO*count rate is due to lower energy electrons. However, the efficiency for detecting the total electron energy will be correct.

TABLE II-2

Intensity vs. Energy Calibration of 5/13/72

Beam Energy (Measured 5/12/72)	$I_{peak}(E)$ Electrons/cm^2 sec.	$I_{>.16}(E)$ Electrons/cm^2 sec.
.111	2.66 ± .16	same
.132	3.07 ± .15	same
.154	4.67 ± .15	same
.177 ± .007	5.94 ± .14	same
.197	8.15 ± .15	same
.218	9.09 ± .15	same
.240	10.20 ± .24	same
.270 ± .008	11.53 ± .24	same
.324	16.31 ± .29	same
.430	25.4 ± .3	25.7 ± .3
.537	35.2 ± .4	36.0 ± .4
.643	43.6 ± .4	44.4 ± .4
.853	57.2 ± .5	58.4 ± .5
1.064 ± .010	65.0 ± .5	66.2 ± .5
1.274	66.0 ± .5	67.6 ± .5
1.490	62.9 ± .5	64.4 ± .5
1.698	55.1 ± .4	56.7 ± .5
1.897	47.4 ± .4	48.7 ± .4
2.119 ± .010	37.5 ± .4	38.4 ± .4
2.340	28.5 ± .3	30.0 ± .4
2.557	19.4 ± .3	20.2 ± .3
2.774	10.36 ± .19	11.14± .25
2.987	4.86 ± .09	5.15± .13
3.194 ± .010	1.41 ± .05	1.65± .13

NOTE: UNCERTAINTY IN BEAM ENERGY DUE ONLY TO ACCURACY OF DETERMINING MEAN OF TOTAL ENERGY DISTRIBUTION. UNCERTAINTIES IN I(E) DUE TO STATISTICS ONLY.

FIGURE II-B

INTENSITY vs ENERGY

(Calibration of 5/13/72)

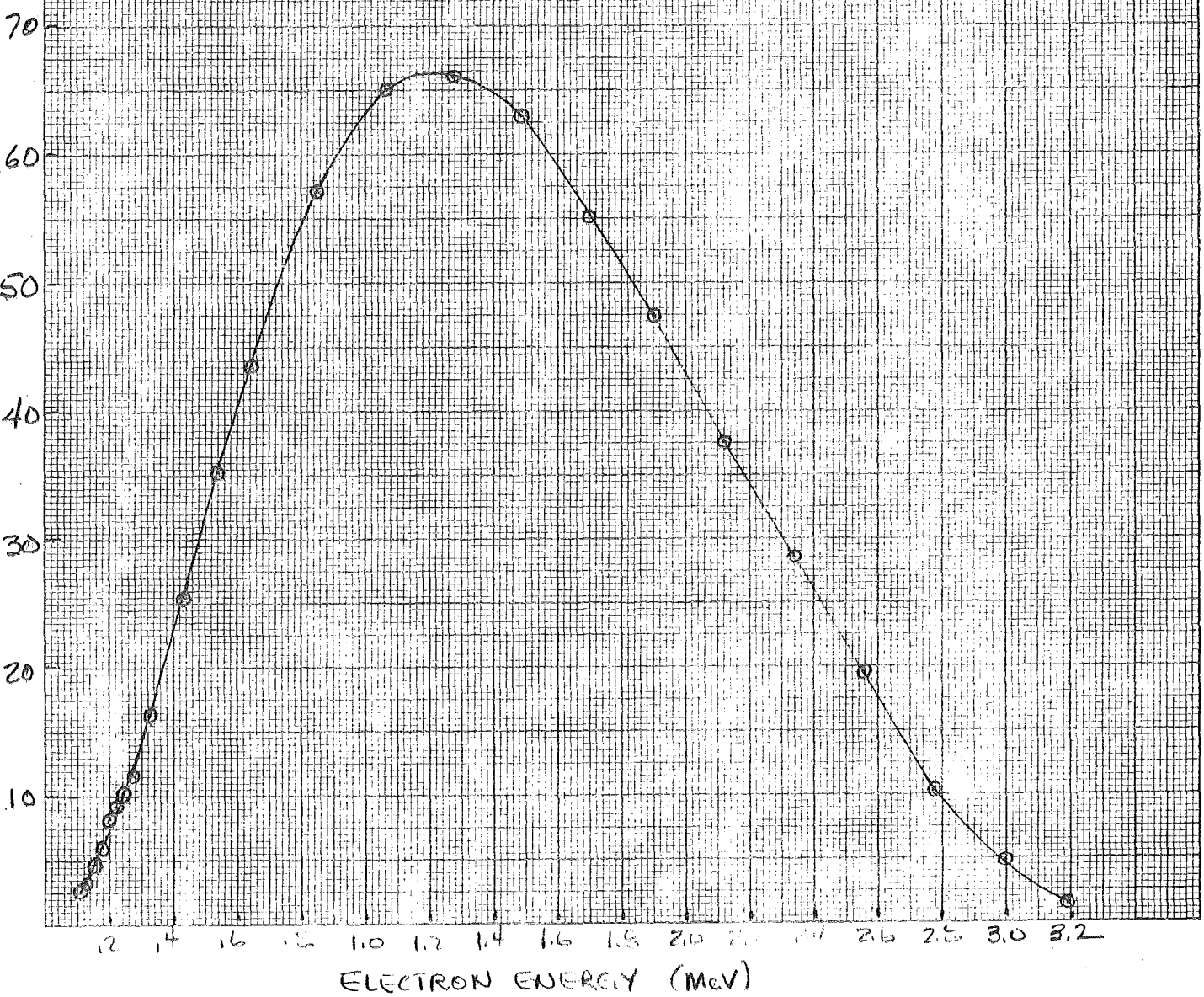

II.

B-3 Angle of the Detector Stack with Respect to the Beam

Measurements with a highly collimated scintillator showed that the β-spectrometer beam was at a $9^{o} \pm .5^{o}$ angle with respect to the vertical. Conveniently, the EIS stack is at a 9^{o} angle with respect to the normal to the front panel of the EIS unit. The instrument was mounted in the spectrometer so that when the front EIS panel was parallel to the baseplate, the beam was at a 0^{o} with respect to the detector stack. The maximum angles available were limited by the bell jar, and varied from calibration period to calibration period. (See Table #II-1).

Unfortunately, the indirect angular readout system was found to lead to systematic errors of up to $\sim 3\text{-}4^{o}$ in the EIS rotation angle, due to slop in the worm-gear arrangement. The magnitude of this problem was not realized until after all IMP-H calibrations were completed. A surrogate EIS instrument, of exactly the same weight and center of gravity was used to calibrate the angular read out error. Figure #II-4 shows the relation between the actual angle θ_A and the angle indicated by the indirect readout system θ_R (the settings at which IMP-H measurements were taken). Notice the asymetry with respect to the angle of the last previous setting indicating some inertia in the readout error.

In all data analysis, the value of θ_A, as taken from Figure #II-4 was used, except for occasional minor adjustments when other data was available. The accuracy of the corrected θ_A values is probably typically $\pm .5^{o}$, although occasional errors of as much as $\pm 2^{o}$ may be present. The effect of this uncertainty is greatest on the calibration of the highly collimated narrow geometry response. In the β calibrations of IMP-J an improved direct angular readout was used, having an accuracy of $\sim \pm .1^{o}$. However, the beam angle may vary by as much as $\pm 0.5^{o}$.

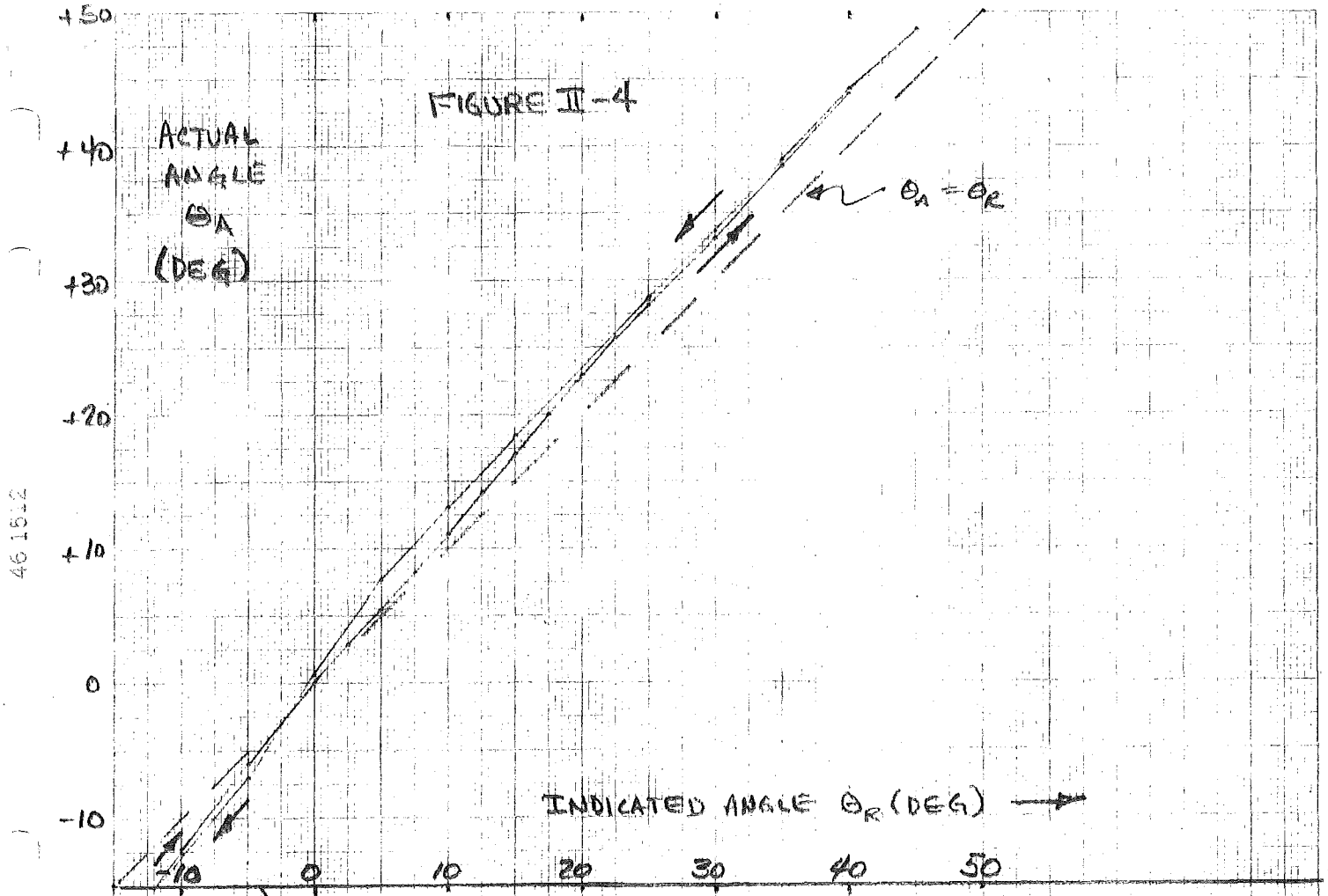

FIGURE II-5

LONG TERM MAGNET CALIBRATION DRIFTS (Relative to 5/14/72)

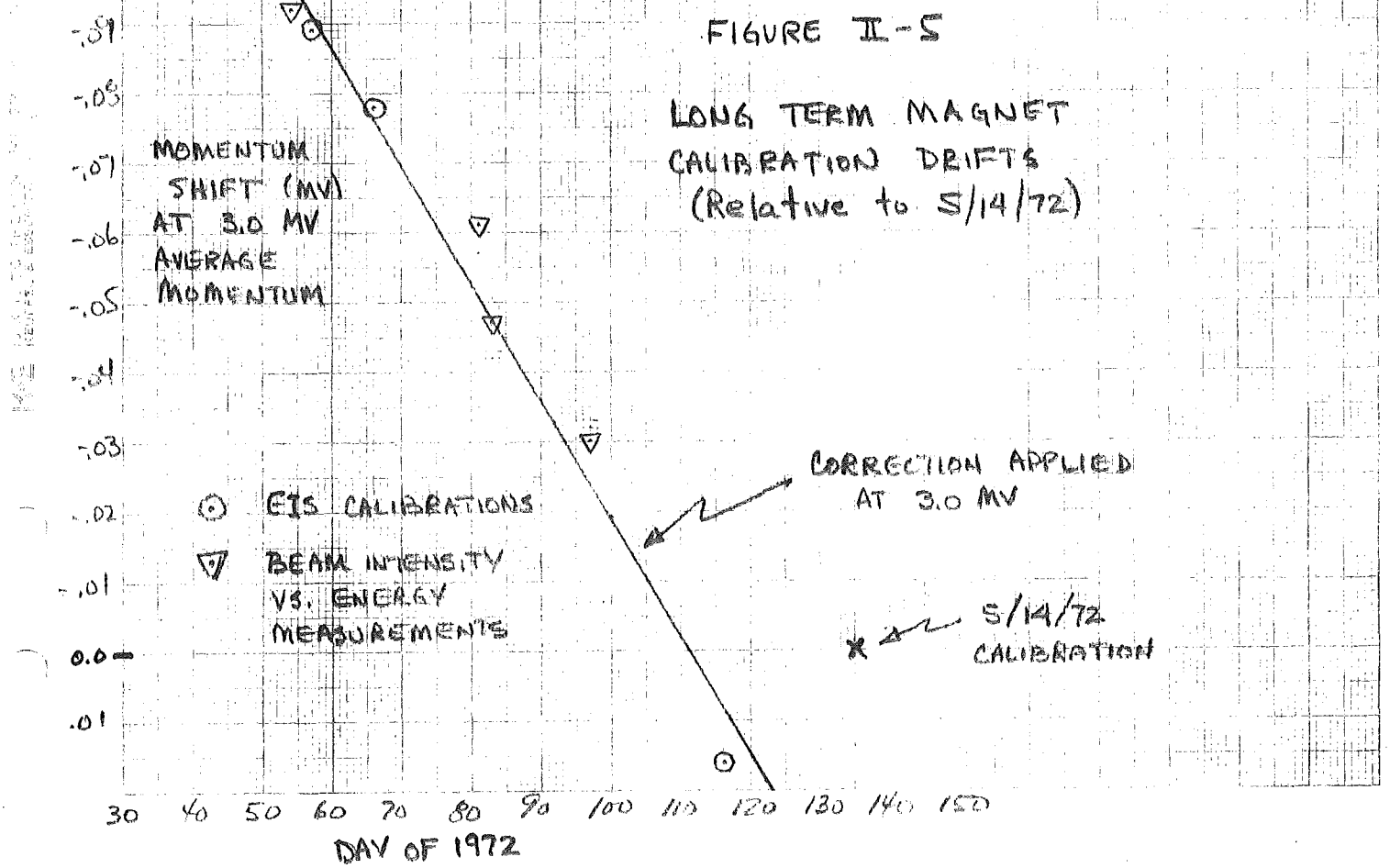

II.

B-4 Temperature Effects

A comparison of high energy (> 2.5 MeV) runs taken at different times indicated sizable drifts in the high energy calibration. These were traced in part to the Bell #620 Hall probe electronics (not the probe itself) whose gain was found to be temperature sensitive. Temperature chamber tests of the Hall Probe electronics showed a gain drift of ~ + .067%/^{o}C. A temperature change from 20^{o}C to 30^{o} C (not uncommon during 24 hour runs) leads to a change in beam energy of only ~ - 24 kev at 3 MeV, but the change in beam intensity is ~ + 11%, since the intensity is a sensitive function of energy at high energy (see figure #II-3). Using the average of the maximum and minimum temperatures measured by the EIS to measure temperature drifts, since this information was always available, all runs were normalized to 24^{o} C (the temperature during the 5/14/72 magnet calibration). The EIS temperature was found to be ~ 4^{o} warmer than the Gaussmeter temperature on the average. A corrected beam momentum was calculated, and a corrected beam intensity interpolated from Table #II-2.

B-5 Long Term Drifts in the Magnet Calibration

Sizable long term shifts in the magnet calibration were observed to occur over the span of the IMP-H β calibrations. These shifts were evident both in the measured beam energy (at the same gaussmeter reading) and in the beam intensity vs. gaussmeter reading curves. At the time of the initial analysis of this data the nature of these drifts was not understood, and a semi-empirical correction was derived and applied to obtain corrected beam energies and intensities. For a given momentum P (from the 5/14/72 Magnet calibration) the average shift in momentum ΔP

on day D of 1972 was found to be $\Delta P = -(0.0627 - .00563 \cdot D) \cdot P$. Figure # II-5 shows this rather curious behavior. The ΔP values in Fig. # II-5 represent the average correction necessary to map intensity vs. energy (1.8-3.0 MeV) curves for any given day onto the 5/13/72 calibration. Similar behavior was also observed at lower energies ($\lesssim$ 1 MeV) where the beam energy can be measured directly by the EIS.

From the corrected momentum $P' = P + \Delta P$, a corrected beam energy and interpolated intensity (Fig. #II-3) were calculated. This correction was found to reduce the average deviation between the expected and actual beam momenta for various calibration periods by a factor of ~ 5. The corrected beam momenta during any single run are probably in error by $\lesssim 1\%$ after this correction has been applied.

The major source of these long term calibration shifts was discovered during the IMP-calibrations. It was found that the placement of peripheral magnetic material (e.g. motors, C-clamps, transformers) near the beam path leads to perturbations in the local B field with resulting shifts in both the beam momentum and angle (as measured at the stack location). This rather obvious effect implies that in future calibrations and measurements, the immediate environment of the spectrometer should be strictly controlled and reproduced. It now appears that the momotonic time dependence in Fig. # II-5 is not physically meaningful, but is the result of introducing more and more pheripheral equipment (e.g. cooling fans etc.) into the spectrometer environment in succeeding calibration periods. It is also likely that significant calibration shifts might have occurred between successive runs on the same day when the magnetic environment was suddenly altered.

II.

C. EIS PROBLEMS AND IDIOSYNCRASIES

During the course of the β-spectrometer calibrations a number of malfunctions of the EIS instruments and GSE occurred. In addition, several idiosyncrasies of the instrument that affect the interpretation of electron data were discovered. This section describes the more important of these problems.

1. Noisy or Disabled Detectors

A number of detectors exhibited serious noise problems (> 10 sec^{-1}) and in some cases had to be disabled. There instances are noted in the IMP-H β-spectrometer run summary. Noisy detectors will produce abnormally high chance-coincidence rates and give erroneous range information (for example D0D8 coincidences when D8 is noisy), while disabled detectors enhance the apparent rate of some ranges, and eliminate others.

The analysis to date has included only those runs where disabled detectors have no significant effect. For example DØ events are not affected when D1 is disabled if the electron energy is $\lesssim .6$ MeV.

2. Noisy Rates

During a number of runs (principally on 3/9/72) some or all of the normalized rate data was bad although range and pulseheight data seemed unaffected. This problem seems to have been caused by a bad connection between the EIS instrument and GSE. Any runs showing evidence of abnormal rates (e.g. non-negligible PLO or PHI rates, or an inconsistent ELO, EHI or NEUT rate in one sub-com state) should be checked individually. Alternative modes of event rate normalization are sometimes possible in these cases.

II-C-3.

The D0 → D10 crosstalk seen in IMP-H flight data appears to be of a different nature. Although the D10 rate scales with the D0 rate (D10 ~ .1 D0 at high rates), the D0* rate appears normal with (D0 - D0*) ~ 10/sec for D0* rates ranging over many decades. The excess rate of ~ 10/sec is consistent with the singles rates of all other detectors due to high energy cosmic rays and interaction secondaries that also trigger D11. Because of other uncertainties, it is difficult to prove that D0* events are not being lost due to D0 → D10 cross-talk, but there is no evidence to date to invalidate this assumption.

4. D0 Channel 0 Events

Because of small timing uncertainties in the D0 rundown, events in which the D0 energy loss is between .158 and .326 MeV may be read out as either channel 0 or channel 1. Unfortunately D0 channel 0 events (D0 ch0) cannot be easily distinguished from readouts where there was no new event and the preceeding event had range D0. Although it is expected that the ratio of valid D0 ch 0 to D0 ch 1 events should be constant, it is possible that this constant is temperature dependent. In flight data it is possible to identify a vast majority of D0 ch 0 events by checking whether the range or sector changed from the preceeding event.

Identical sectors for adjacent readouts will occur only on the order of ~ 1/8 of the time because of the relation of the S/C spin rate (~ .76 sec^{-1}) and the EIS readout rate (1/.64 sec^{-1}). By accepting all D0 ch 0 events with a new range or sector, and rejecting those with the same sector as preceeding D0 range events it is found that (D0 ch 0)/(D0 ch 1) $\simeq$ .56 during quiet time. This ratio appears to give consistent D0* rate and event fractions.

II-C-4

An initial determination of the (D0 ch 0)/(D0 ch 1) ratio in the β-calibration data measured the (D0 ch 0)/(D0 ch 1) ratio in D01* events, and found .097 ± .010 . Some of the "Electan" output has been corrected with this number. Flight data indicates that the ch 0/ch 1 in D01* events is not equal to that in D0 events. Therefore the wide geometry electron efficiences (Section IV) were recorrected using the flight ch 0/ch 1 ratio of .56, with no apparent inconsistencies.

Future analysis of both calibration and flight data may shed more light on this problem. The possible error arising from it is less significant when it is realized that the interpretation of an electron channel whose width (ΔE = .17 MeV) is the same as its threshold ($T \simeq .16$ MeV) is already difficult; and when the frequent contamination of this channel during quiet times by terrestrial albedo electrons is considered.

5. D5 Offset Shift

Because of gradual and sudden shifts in the D5 calibration, momo-energetic electron spectra taken at different times will not generate the same pulse height from the EIS instrument. (See SRL Internal Report #56). Corrections for this problem make use of D5U, the D5 unstimulated pulse height, as described in Section III-C. In this analysis the D5U correction was applied only to the nearest integral channel, in order to preserve a $\sim$ 41 KeV/channel energy scale. The corresponding energy uncertainty is $\lesssim$ 20 KeV, which is comparable to other uncertainties in the instrument calibration and response.

II-C

6. Miscellaneous Other Problems

Due to computer software problems, electron data recorded during 1/31/72 - 2/1/72 exhibits several anomalies. 1) The four subcom states of the normalized rate block were interchanged. 2) Rates were accumulated over only ~ 1/20 of the nominal time period, resulting in rather poor statistics. 3) High rates in a single rate line (e.g. D11) produced anomalously high dead time in other rates, accumulated during the same subcom state. A modified version of KENTAN (A.D. Petruncola) allows for the first two of these problems. Because of these complications, and the limited coverage during these runs, data from the 1/31/72 - 2/1/72 period was not included in this analysis.

A temporary modification to the FTU in mid-February, 1972 affects the interpretation of rate data accumulated from 15 Feb, 1972 to 15 March 1972. The major effect is the loss of the PEN rate during this period (See memo by G. Hurford dated 3/27/72). Although this period coincides with that during which D0 → D10 cross talk was observed, the connection is not apparent.

During the runs of 3/9/72 - 3/10/72 a Th α-source and a B_i^{210} electron source were mounted in the β-spectrometer tube for the purpose of producing monoenergetic calibration standards. Although shielded during the electron runs, significant γ-ray background was evident during low intensity electron runs, necessitating a time dependent background correction for this period. In retrospect, the introduction of additional sources of background during instrument calibrations is not adviseable unless necessary.

II - D

D. Calibration Scheduling

Several general principles motivated the overall calibration run schedule. Approximately 20 beam (.1 - 3.2 MeV) energies were selected within the limitations of the EIS instrument and the β-spectrometer. The beam energies were spaced so as to provide greater coverage at low energies where the EIS energy resolution is at a maximum. For each beam energy, calibrations were performed in 5^{o} steps from 0^{o} to 45^{o} (see section II-B-3). The priority disable switch on the GSE was implemented so as to give ~ 2/3 of the time to wide geometry and ~ 1/3 to narrow geometry during each run. Periodic background runs (beam off) were also scheduled.

The limited availability of the EIS for particle calibrations forced compromises in the planned schedule. In general, relatively less time was spent at low energies (≤0.6 MeV), where only single detector events are observed. Angular accumulation times were weighted approximately by the instrument's differential geometry factor, with additional time spent at $\theta = 0^{o}$ where interpretation of the response is most straight-forward. An attempt was made to selectively cover the entire E, θ ranges in the initial calibration periods in the event that further calibrations were pre-empted by unforseen problems in the overall EIS testing and calibration schedule. Later runs concentrated on filling in gaps, redoing problem runs, and improving statistics. Unfortunately, time limitations prevented the completion of all of these objectives. In addition, the various instrumental problems described in sections II-B and II-C have complicated the combining of data accumulated at different times over the ~ 4 month calibration period. Section VI comments on calibration planning for future instruments.

II - E

E. Summary of Recorded Data

All EIS data accumulated during the β-spectrometer calibrations were recorded on 7-track tape (1 file per run) using the Varian 520i program BTP-2 (Curt Widdoes). In addition, information pertinent to each run (energy, angle, time, etc.) was recorded in the IMP-H Instrument Log Book. Teletype output listing a representative event sample is also available for most runs.

From the individual data tapes, two identical master summary tapes, HBETA1 and HBETA2, were prepared. A bound summary (yellow binder) of the header and trailer records for all files on these tapes is available. All runs have been processed through KENTAN, producing normalized rate and range distribution summaries, and in many cases one and two dimensional pulse-height plots for individual ranges. This bound output is also available, arranged sequentially by time. A run summary indexed by energy, of all runs and the problems encountered has been prepared by Patrick Nolan.

Further processing of a majority of runs has utilized ELECTAN (normalized one-dimensional energy spectra, stored on Tapes BETAN1, BETAN2) and ELEFIT (integrated and differential geometry factors for range distributions and energy spectra). The output of these programs is described in the next section.

III. DATA ANALYSIS

A. General Procedure

An outline of the steps comprising the analysis procedure for calibration and flight electron data is shown in Figure III-1. This figure also contains the parallel steps involved in the analysis of the γ-ray calibration and flight data, described in detail in Internal Report #54.

The programs BTP2 and KENTAN have been described in writeups by Curt Widdoes and Alex Petruncola.

ELECTAN (labeled KETEST in some outputs) is an extension of KENTAN. ELECTAN produces normalized one-dimensional total energy loss spectra from 0 -4 MeV for events of all ranges, along with normalized range distribution data. The method of combining two dimensional pulse-heights into a one-dimensional energy spectrum is described in section III-C, and the absolute rate normalization method is described in III-B. ELECTAN uses the algorithm described in the KENTAN writeup for dead time corrections to the normalized rates. Corrections are also applied for D0 channel 0 events and D0 → D10 crosstalk (see section II-C). All ELECTAN output was stored on 9-track tapes (one file for each run) named BETAN1 and BETAN2 for analysis by ELEFIT. In addition to the usual multidetector ranges (01, 013 etc), ELECTAN produces energy spectra for various range combinations. These are defined in III-F.

ELEFIT reads from BETAN1 and BETAN2 the runs performed at each energy; calculates, fits, and integrates the angular response ($0 \leq \theta \leq 45^{o}$); and produces geometrical factors for rates, range distributions, and the individual channels of all energy spectra (see Section III-D). Corrections are applied for the decay of the Ru^{106} source, energy drift of the beam with time, and temperature drift of the Hall probe see Section II-B). Background

III-A

spectra, averaged over runs with the beam off, are substracted from all rates, and all ranges and spectra involving $\leq$ 2 detectors (see Section III-D). Calcomp plots can be produced of the effective detection area $A(\theta)$ for selected rates and ranges. Examples of ELEFIT output are presented in Section IV. The ELEFIT output can be used to construct response matrices, which summarize the geometry factors for electron detection as a function of energy. A wide geometry response matrix is described in detail in Section IV-F.

The current procedure for analyzing flight electron data makes use of a STRIP tape produced from the IMP-H Abstract Data Tapes by the PDP-11 program STRIP (Alex Petruncola). ELCOR (Pat Nolan) reads the STRIP tape, corrects for γ-ray and proton background, and proceduces card output appropriate for MIFEL. MIFEL uses calibration response matrices to unfold the corrected flight data and produce electron differential energy spectra. The matrix inversion method employed is outlined in Section III-E.

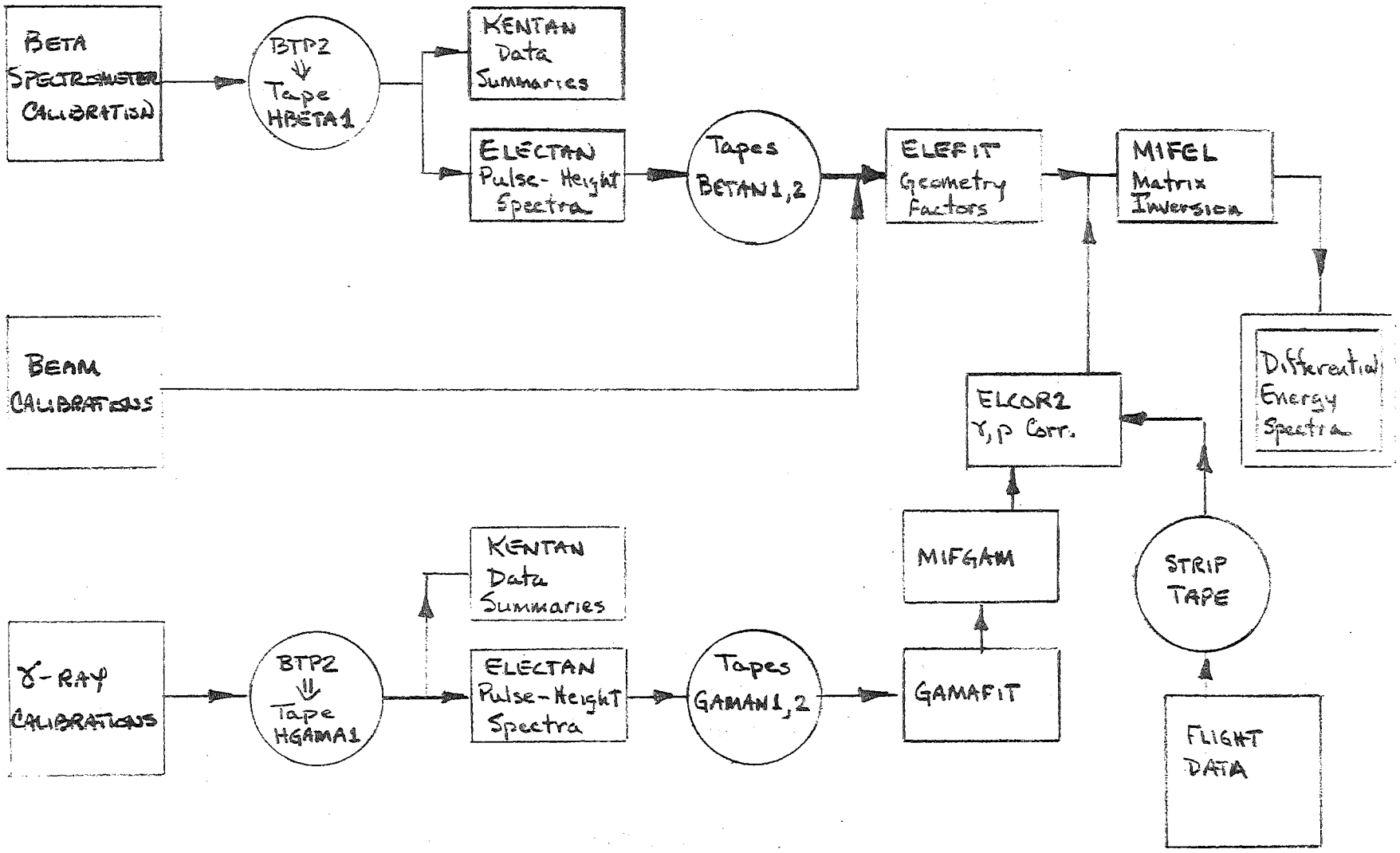

FIGURE III - 1 DATA ANALYSIS OUTLINE

III.

B. Normalization of Event Rates

The normalized rate of events of a particular range I and channel number K (called $R(E,\theta,I,K)$) was calculated in ELECTAN as follows:

Let: $Q(E,\theta,L)$ = EIS normalized rate of type L due to electrons of energy E at angle θ.

$N(E,\theta,I,K)$ = # of analysed events of range I, channel K.

$TN(E,\theta,L) = \sum_{I} N(E,\theta,I)$ = all analysed events of rate L

then $R(E,\theta,I,K) = \frac{N(E,\theta,I,K)}{TN(E,\theta,L)} \cdot Q(E,\theta,L)$

The uncertainty SR in R was found by combining in quadnature the uncertainty SQ in Q with the uncertainty in the fraction $N/TN \pm [N(1-N/TN)]^{1/2}/TN$ (Bevington, 1969).

Table III-1 shows the EIS rates used to normalize various ranges.

Table III-1 Normalization Conventions

Event Range	EIS Rate used to normalize
0,01,....0-9	D0*
5,56,....5-9	(EL0 + EHI ≡ ETOT)
7,67,....6-9	NEUT
5T 5-T	PEN (when available)

III.

C. Energy Definitions

In this initial analysis of the EIS electron calibrations a one dimensional total energy loss scale was defined for simplicity. For multiple detector events, the A and B pulse heights were combined to form a total energy loss sum with ~ .165 MeV resolution. Additional corrections were applied to account for finite channel width when more than 2 detectors were triggered. For example a D013 range event having B = 1 could result from $.16 \lesssim E_1 \lesssim .325$ MeV and $.325 \lesssim E_3 \lesssim .49$, MeV or $.325 \lesssim E_1 \lesssim .49$ MeV and $.16 \lesssim E_3 \lesssim .325$ MeV (see Internal Report #56). A reasonable estimate of the total energy lost in D1 and D3 is therefore ~ .165 MeV greater than the threshold for triggering D1 and D3 with B = 1. For this reason an additional ~ .165 MeV was added to the total energy sum for every 2 detectors contributing to the B register sum.

Generalizing this, let $K \geq 1$ be the total energy index in units of ~ .165 MeV and NS be the number of detectors in the B register sum. The general principle followed was to set K = A + B + NS + NS/2 where the NS term is necessary since detectors 1,3,4, and 6-9 have B = 0 for energy losses $\gtrsim$ .16 MeV. The NS/2 term follows the integer truncation rule (e.g: NS = 5 ⇒ 5/2 = 2). The advantage of this total energy definition is that energy loss spectra from several different ranges can be combined without introducing significant systematic effects. A number of these combined range spectra have been defined and calibrated (see Section III-F). We now consider the application of this definition to the various electron and γ-ray analysis modes.

III-C.

Wide Geometry

Two exceptions to the definition K = A + B + NS + NS/2 occur in wide geometry. 1) A = 0 is treated as A = 1 since channel 0 in D0 is equivalent to channel 1. 2) When D5 is included in the B sum the instrument follows the rule B_5 = (D5 + 2)/4. In order to make B_5 = 1 when $E_5 \approx$ .325 MeV NS has been reduced by (D5U+6)/4 when D5 was in the B register sum*. D5U is the unstimulated D5 pulseheight (see SRL-IR#56).

Neutral Events

For neutral events K = B + NS + (NS-1)/2 was used. This adds the same $\sim$ .165 MeV correction to 3 detector neutral events (e.g. D678, NS = 3) as in wide geometry (e.g. D013, NS = 2) and narrow geometry (e.g. D567, NS = 2.) Note that because D7 has an extra channel between .16 and .325 MeV (see CALAN Output For D7 in SRL Internal Report #56) the neutral energy loss spectrum will be offset by $\Delta K \sim 1$ from the wide and narrow geometry spectra for the same actual energy loss. Again this offset is unimportant if flight and calibration data are treated in a similar fashion.

Narrow Geometry

In narrow geometry an extra complication is introduced because D5 has $\sim$ .041 MeV channel width. For D5 single events a separate spectrum was established having index K5 and $\sim$ .041 MeV channel width. The definition K5 = A - D5U gives (K5 = 8) $\tilde{-}$ .326 MeV, such that K5/4 $\tilde{\sim}$ K for energy losses $\geq$ .326 MeV. K5 values <8 will be non-linear (see SRL IR #56).

*The above correction should more properly have been to reduce K by (D5U + 6)/4 rather than NS. The error of $\sim \Delta K = 1$ for 01345 events is not significant if flight and calibration data are treated in a similar fashion.

III-C.

For multiple detector narrow geometry (NG) events we define K = K5/4 + B + BS + NS/2 - 1·D7. The corrections of $\Delta K = -1$ when D7 is triggered takes into account the extra D7 channel and alligns the NG and WG spectra in an approximate manner.

Although in general the above definitions give $E(K) \simeq 0.165K$ MeV as the threshold for channel #K, there are seen to be differences of up to $\sim .165$ MeV between various ranges (more typically $\pm .080$ MeV). Note however that if flight data is analysed in the same manner as the calibration data, and if flight energy spectra are deduced by comparison with the calibration response, the absolute calibration of E(K) for any particular range is immaterial.

D. Geometry Factor Determination

The geometry factor $G_i(E)$ for detection of electrons of energy E with analysis mode i (where i can be a rate, range, or individual channel) was determined by ELEFIT in the following manner.

Let: $I(E)$ = Electron intensity at D0 ($cm^{-2} \cdot sec^{-1}$)

$R_i(E,\theta)$ = Rate of events of type i (range or channel number) at angle θ (sec^{-1}), corrected for background

Then $A_i(E_1\theta) = R_i(E,\theta)/I(E)$ is the effective electron detection area

and $G_i(E) = 2\pi \int_0^{\pi/2} A_i(E,\theta) \sin\theta d\theta$ is the geometry factor.

In practice $R_i(E,\theta)$ was measured at $\lesssim 10$ not always evenly spaced angles over $0 \leq \theta \leq \pi/4$. It therefore became convenient to fit $A_i(E_1\theta)$ vs θ,

III-D.

$$A_i(E,\theta) \simeq \sum_{n=0}^{4} C_n P_n(\cos 4\theta)$$

where $P_n(\cos 4\theta)$ is a Legendre polynomial or order n. The $P_n(\cos 4\theta)$ are a complete set over the internal $0 \leq \theta \leq \pi/4$

Then

$$G_i(E) = 2\pi \int_0^{\pi/4} \sum_{n=0}^{4} C_n P_n(\cos 4\theta) \sin\theta \, d\theta$$

$$= 2\pi \sum_{n=0}^{4} C_n D_n \qquad \text{where } D_n = \int_0^{\pi/4} P_n(\cos 4\theta) \sin\theta d\theta$$

is constant.

Examples of $A_i(E,\theta)$ are shown in Figures IV-1. Reasonable fits were achieved for both narrow and wide geometry.

Uncertainties were treated as follows: The uncertainty $SA(E,\theta)$ in $A(E,\theta)$ combines the statistical uncertainty SR in R with an assumed 2% uncertainty in the beam momentum. Uncertainties in $G_i(E)$, which are difficult to evaluate from the Legendre polynomial fits, were taken from the error analysis of a separate numerical integration (trapezoidal), routinely performed in parallel.

Plots of $G_i(E)$ vs E for the D0 singles and ETOT $\equiv$ ELO + EHI rates were checked for consistency. The individual points were found to vary from a smooth curve by $\sim \pm$ 2% (D0) and $\sim \pm$ 5% (ETOT). These deviations are in general greater than the calculated uncertainties, and undoubtedly represent systematic errors

III-D.

introduced when data from different calibration periods was combined. It was found that the consistency between points based mainly on data from the same calibration period was much better ($\sim \pm 1\%$, $\pm 2\%$) than the overall consistency. For wide geometry, the variations between calibration periods undoubtedly arise mainly from uncertainties in the beam intensity and energy (Section II-B-5) while for narrow geometry the angular uncertainty (Section II-B-3) probably dominates.

To correct for these deviations, the wide and narrow geometry data were separately renormalized to smooth curves through the DO and ETOT points. Greatest weight was given to points based mainly on the 4/25/72 calibration. It is undoubtedly possible to gain further understanding of this complex problem by comparing individual runs from different calibration periods, and by studying the IMP-J data, where systematic effects were under better control.

E. Least-Squares Technique for Obtaining Electron Energy Spectra

Because of electron scattering effects and finite instrumental resolution, an isotropic monoenergetic flux of electron will in general produce a distribution of energy losses within the detector system, spanning the range from the $\sim$ .16 MeV threshold up to the total electron energy (see examples in Section IV-D). We therefore require a quantitative method of unfolding observed energy loss distributions to obtain the actual electron energy spectrum. The least-squares method employed here is described in detail in Trombka, and was employed by J. L. Lupton in Internal Report #28.

III-E.

We select NJ energy intervals spanning the instrument response. Let F(J) be the electron flux ($cm^{-2}sec^{-1}sr^{-1}MeV^{-1}$) in the energy interval centered at E(J) of width $\Delta(J)$, where $1 \leq J \leq NJ$. Let $C(K) \pm \sigma(K)$ be the number of counts in channel K during time t, where $1 \leq K \leq NK$, and $NK \geq NJ$. Let the matrix element M(K,J) be the geometry factor for producing a count in channel K with an electron of energy E(J). Thus M(K,J) contains all information about the instrument response.

It then follows that

$$C(K) = t \cdot \sum^{NJ} \Delta(J) \cdot F(J) \cdot M(K,J)$$

We wish to invert this to obtain F(J). This is accomplished (see Trombka), by defining the new matrices

$$\omega(K,K) = \left[1/\sigma(K) \right]^2 \qquad \text{(diagonal)}$$

and

$$m(I,J) = \sum_{L}^{NJ} M^t(I,L) \sum_{K}^{NK} \omega(L,K)M(K,J)$$

and the new vector

$$c(L) = \sum_{K} M^t(L,K)\ \omega(K,K)C(K)$$

where M^t is the transpose of M. Then

$$F(J) = \frac{1}{t \cdot \Delta(J)} \sum_{L} M^{-1}(J,L)c(L)$$

III-E.

Assuming that the instrumental response M(K,J) is known exactly, the uncertainty S(J) in F(J) given by

$$S(J) = \frac{1}{t \cdot \sigma(J)} \left[m^{-1}(J,J) \right]^{1/2}$$

where m^{-1} is the inverse of M.

The advantage of this approach is that the number of outputs F(J) ($J \leq NJ$) can be smaller than the number of inputs C(K) ($K \leq NK$), allowing the redundant information available from the various detector ranges to be easily incorporated. The example in Section IV-F should make this clear.

The above procedure for obtaining electron differential energy spectra is accomplished by MIFEL, which then fits the F(J) to a power law of the form $F(K) = A \left[E(K) \right]^{-\gamma}$.

F. Definitions and Conventions

1. Reoccuring notation used in this report

E	Electron kinetic energy
W	Electron total energy = $E + M_e$
P	Electron momentum
M_e	Electron rest mass
$R(I,K,E,\theta)$	Event rate in range I channel K due to electrons of energy E, at angle θ
θ	angle with respect to the telescope axis
K	energy index (channel number) (~ 165 KeV/channel)
K5	D5 high resolution energy index, (~ 41 KeV/channel)

III-F.

$A_i(E,\theta)$	Effective detection area for type i events
I(E)	Beam intensity at D0 in $cm^{-2}sec^{-1}$
T(K)	Threshold of channel K in MeV
$G_i(E)$	geometry factor
Dabc	detector range abc (e.g.D013)

2. EIS Event Type Definitions

Name	Definition
D0*	D0 $\overline{D10}$ $\overline{D11}$
D01*	D0 D1 $\overline{D10}$ $\overline{D11}$
CM0	Common D0* events (all detectors triggered are sequential)
CM01	Common D01* events
UNO	uncommon D0* events
UN01	uncommon D01* events
0*C	D0* corrected for D0 → D10 cross-talk
01*C	D01* corrected for D0 → D10 cross-talk
ELO	$\overline{D0}$ $\overline{D1}$ $\overline{D2}$ $\overline{D3}$ $\overline{D4}$ D5 $\overline{D6}$ $\overline{D10}$ $\overline{D11}$
EHI	$\overline{D0}$ $\overline{D1}$ $\overline{D2}$ $\overline{D3}$ $\overline{D4}$ D5 D6 $\overline{D10}$ $\overline{D11}$
ETOT	ELO + EHI

III-2 Total Energy Spectra Definitions

Analysis Mode	Detector in A Register	Detectors in B Reg.Sum	Energy Loss Index Definition	Corrections
Wide Geometry	D0	D1,D3,D4-9	K = A+B+NS+NS/2	NS reduced by (D5U+6)/4 when D5 triggered
				K increased by + 1 when A=0
Neutral Events	D5U	D6-D9	K = B+NS+ (NS-1)/2	None
Narrow Geometry (NS > 0)	D5	D6-D9	K = K5/4+B+NS+NS/2	K increased by 1 if D7 triggered
Narrow Geometry D5 Singles (NS=0)	D5	D2U	K5 = A - D5U	D5U must be known
			K = K5/4	K = 1 if K5 < 4

IV. RESULTS OF CALIBRATION ANALYSIS

A. Effective Areas for Electron Detection

The effective area $A(E,\theta)$ of a particular detection mode (rate, range, or channel number) was defined in Section III-B to be the ratio of the absolute counting rate (sec^{-1}) to the beam intensity ($cm^{-2}.sec^{-1}$). Figures IV-1 to IV-3 show several examples of plots of $A(E,\theta)$ along with the Legendre polynomial fits produced by ELEFIT. Several effects can be observed in these figures.

1) $A(E,\theta)$ for D0 is approximately constant at ~ 3.5 cm^2 for $0 \leq \theta \leq 15^o$ and $E \gtrsim .6$ MeV. This compares favorably with the D0 wafer area ~ 3.3 cm^2, but is slightly larger, presumably due to contributions from wall scattered electrons.

2) Beyond 15^o $A(E,\theta)$ decreases due to shielding by the D11 housing, which should start cutting in at $\theta \simeq 18^o$.

3) By $\theta = 37.5^o$ D0 is completely shielded for line of sight particles. Note, however, that $A(45^o)$ is still $\sim 7\%$ of $A(0^o)$. Electrons detected at $\theta \geq 37.5^o$ are presumably scattered by the mylar window, and more importantly, the aluminum wall of the scintillator housing.

Figure IV-4 shows $A(\theta)$ for 1.2 MeV electrons in the first version of the IMP-J EIS (identical to IMP-H) where electron calibrations were carried out to $\theta = 80^o$. The wall scattered electron contribution is seen to diminish quickly but not disappear at large angles. Integrating this contribution over solid angle we find

$$\int_0^{\pi/4} A_o(\theta)\,d\Omega \simeq .95 \int_0^{\pi/2} A_o(\theta)\,d\Omega$$

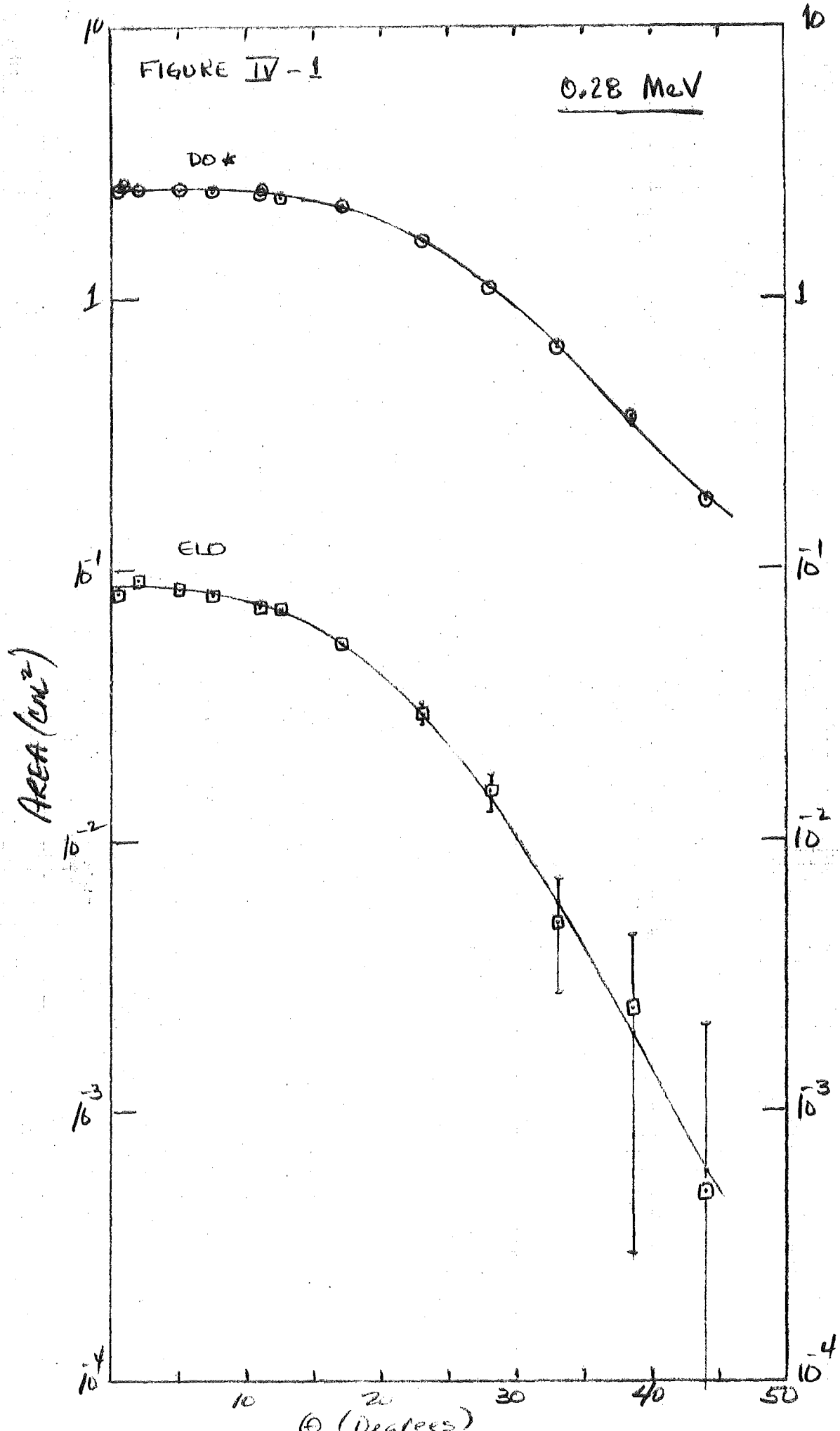
FIGURE IV - 1
0.28 MeV
DO *
ELD
AREA (cm²)
θ (Degrees)
10
1
10⁻¹
10⁻²
10⁻³
10⁻⁴
10
20
30
40
50

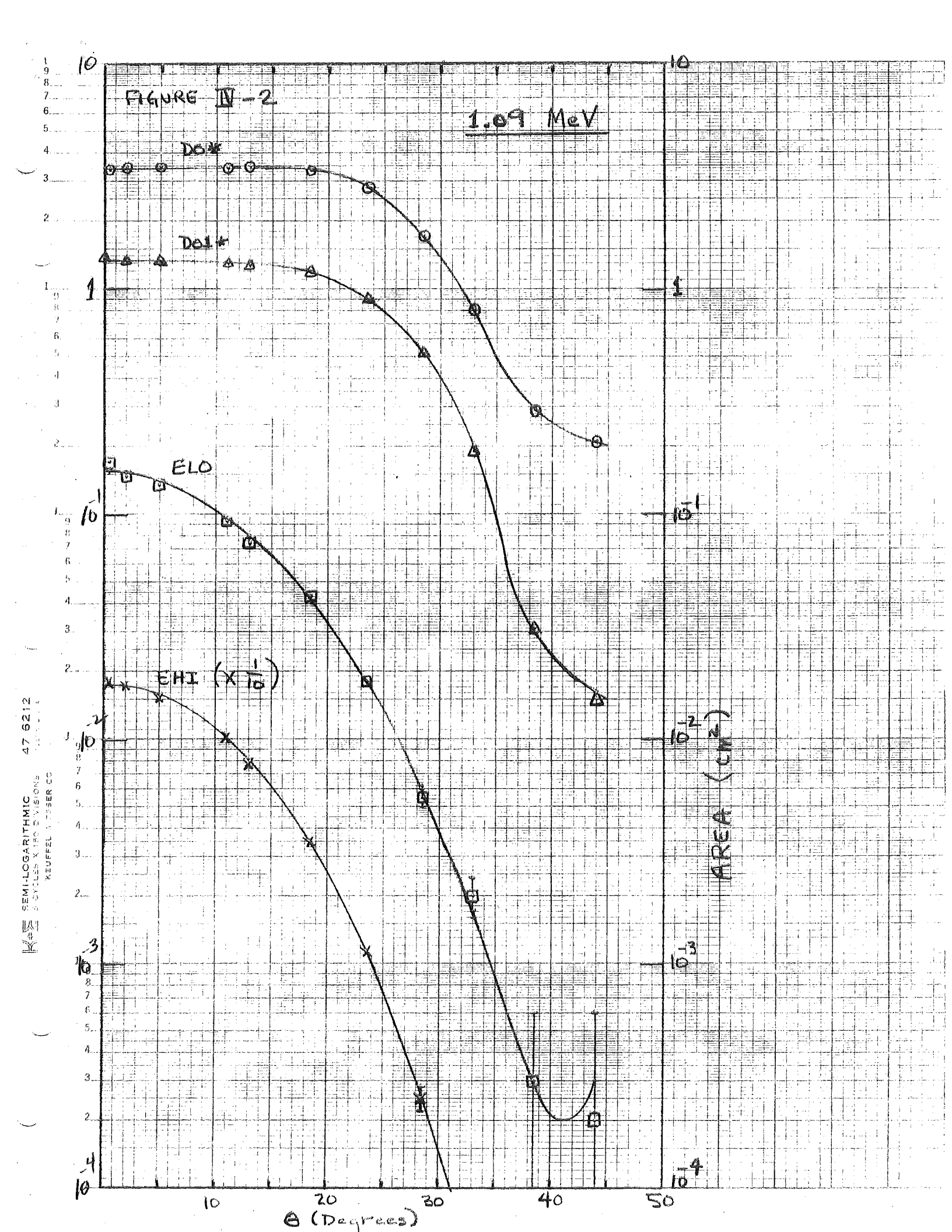
FIGURE IV-2
1.09 MeV
D0*
D1*
E1.0
EHI (X 1/10)
θ (Degrees)
10
20
30
40
50
1
10^-1
10^-2
10^-3
10^-4
SEMI-LOGARITHMIC
5 CYCLES X 100 DIVISIONS
KEUFFEL & ESSER CO
47 6212

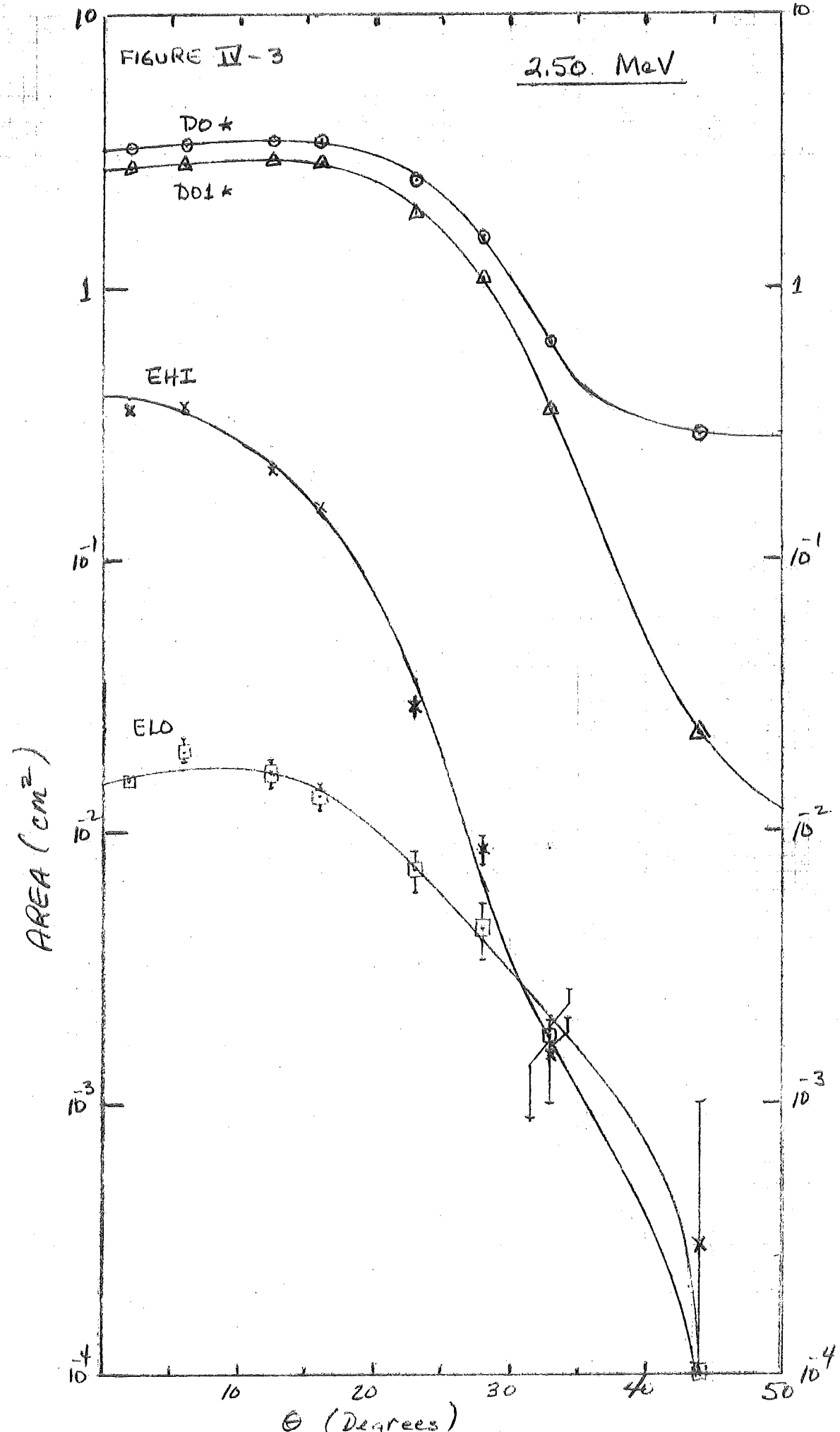
FIGURE IV-3
2.50 MeV
DO*
DO1*
EHI
ELO
AREA (cm²)
θ (Degrees)
10
1
10⁻¹
10⁻²
10⁻³
10⁻⁴
10
20
30
40
50

FIGURE IV-4

IMP-J Angular Response

$\mathcal{E}$ = 1.2 MeV

(Not flight version of IMP-J)

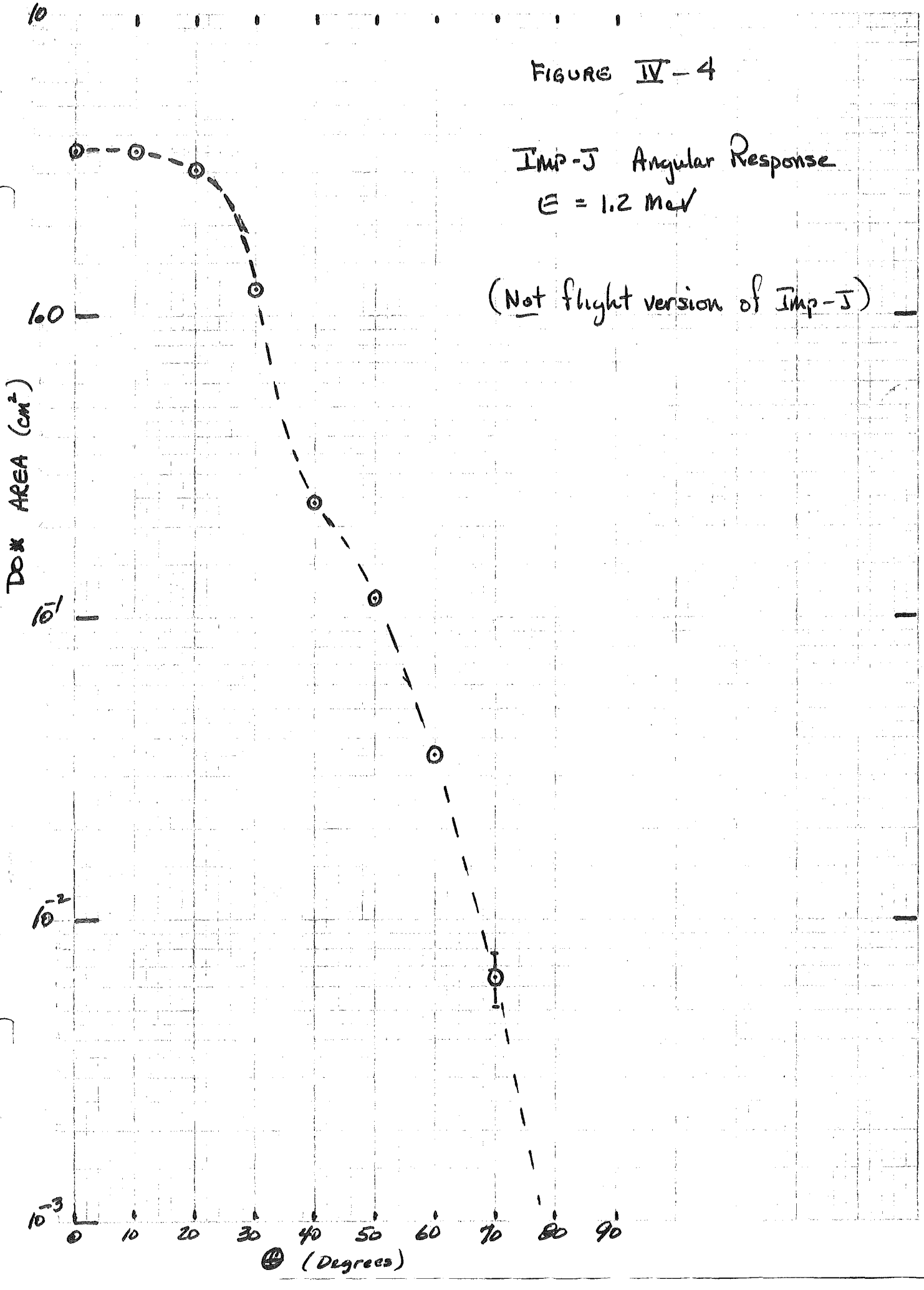

IV. - A.

Thus the integrated IMP-H D0 geometrical factors may be ~ 5% low due to the neglect of contributions at $\theta > \pi/4$. Note however, that a wall-scattered electron will be measured at less than its initial energy and for typical in-flight electron spectra this background contribution will be considerably less than 5% of the count rate from non-scattered electrons at this lower energy. Although $A(\theta)$ is flatter at lower energies (compare $A_o(\theta)$ at 0.28 and 1.09 MeV), the IMP-J results indicate that $G(0\text{-}45^o) \geq .90\ G(0\text{-}90^o)$ for all energies of interest.

John Lupton has made an extensive analysis of the effects of electron scattering in a telescope similar to the EIS (see Internal Report #28 and Lupton and Stone, 1972b). The effects observed here appear to be consistent with his observations.

4) Although the narrow geometry mode is shielded from wall scattered electrons by D0,D1,D3 and D4, there is evidence for scattering effects in D2 and the window. Note that while $A(45^o)/A(0^o) \sim 10^{-3}$ at > 1 MeV, this ratio is $\gtrsim 10^{-2}$ at .28 MeV. Only the window would seem to be able to scatter low energy electrons incident at 45^o narrow geometry. At $\theta \simeq 25^o$, where D2 is visible by line of sight electrons but D5 is not, the $A(25^o)/A(0^o)$ ratio is $\lesssim 10^{-1}$ at 1.09 MeV, and ~ 0.3 at 0.28 MeV.

Table IV-1 contains rough estimates of the mean deflection angle of electrons passing through D2 and the window. (See Rossi, 1951, p.68.) Note that 0.25 MeV electrons are made essentially isotropic by D2. The general trend of electron scattering effects can be predicted qualitatively, but quantitiative calculations will

be of limited accuracy in complex geometrical situations such as these. Extensive calibrations are the only means of accurately determining the response of a low energy electron detector.

5. Several of the $A(\theta)$ distributions contain experimental points that are inconsistent with the trend of the other data. These deviations are presumably the result of inadequate correction for systematic angular and beam intensity uncertainties between different runs.

Table IV-1 Electron Scattering Angles

Electron Energy (MeV)	Mean Deflection Angles D2	Window
.25	$\sim 60^{o}$	$\sim 22^{o}$
1.0	$\sim 19^{o}$	$\sim 7^{o}$
3.0	$\sim 7^{o}$	$\sim 3^{o}$

IV. -

B. Integrated Geometrical Factors for Electron Rates

Figures IV-5 and IV-6 show the electron geometry factors for various EIS normalized rates obtained by integrating the $A(\theta)$ distributions from 0 to $\pi/4$. Also shown is the CMO* curve, made up of events which do not skip detectors (counter-example: 014). The data have been renormalized as described in Section III-D.

Note that while all electrons $\gtrsim 0.2$ MeV are above the ~ 0.16 MeV DO* and ELO thresholds, the detection efficiencies are sensitive functions of energy below $\sim$ For narrow geometry electrons this is presumably because electrons which suffer large angle scattering in D2 do not reach D5. The wide gometry energy dependence may be caused by scattering in the window, as well as the fact that the range of the low energy electrons may not be sufficient to give them access to the full sensitive volume of the detector (see detector depletion profile in Internal Report #45).

The difference between the DO singles and DO* rates at high energies is due to electrons which trigger D11.

C. Range Distributions

Figures IV-7 and IV-8 show the geometrical factors for the wide and narrow geometry ranges as a function of energy. Note that while an individual high energy electron may trigger one of many ranges; given sufficient statistics, the range distribution can be a useful discriminator of the electron energy spectrum. The individual range thresholds appear to be spaced by ~ 0.4 MeV.

Figure IV-5

ENERGY DEPENDENCE OF WIDE GEOMETRY RATES

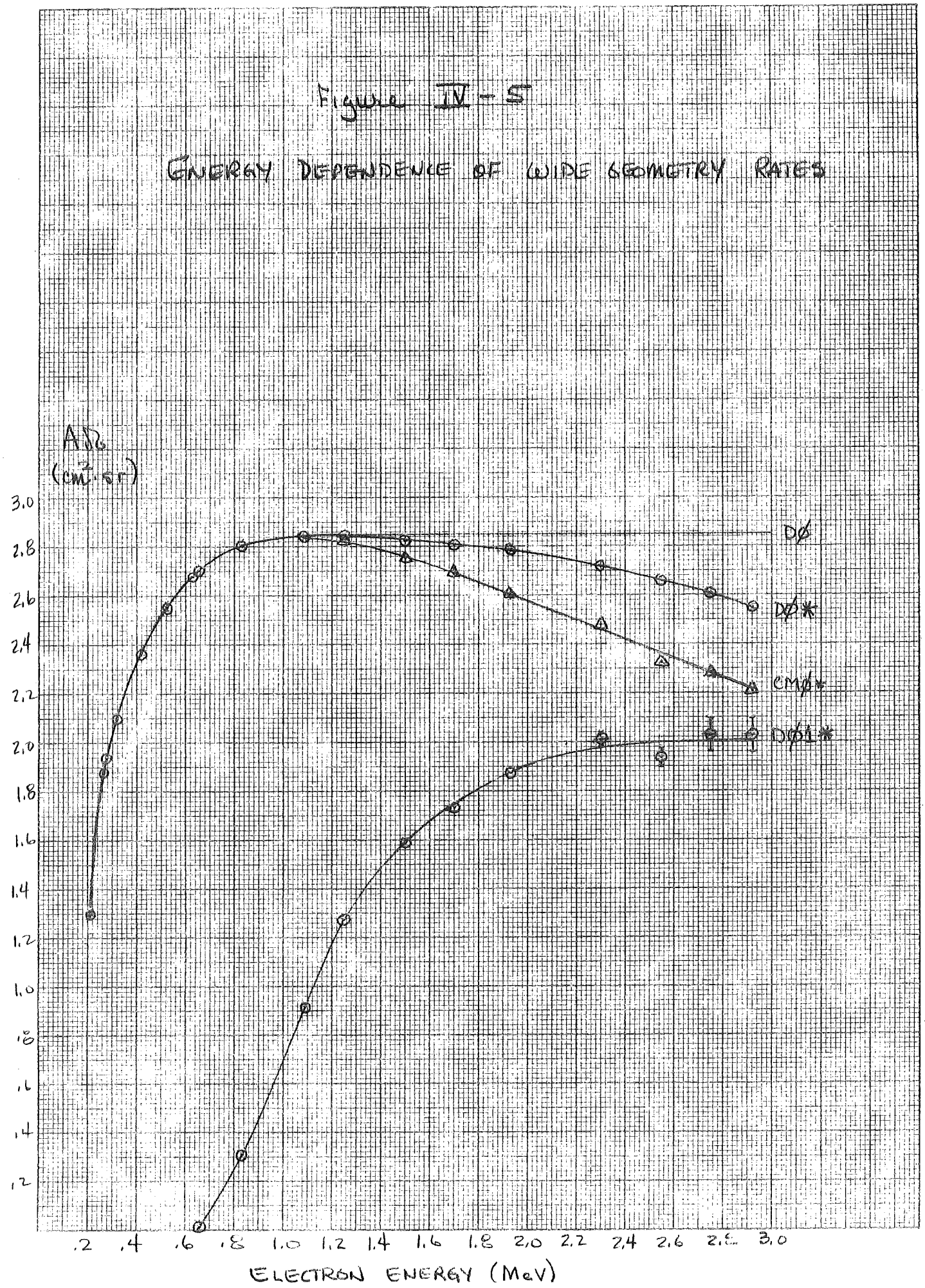

FIGURE IV - 6

ENERGY DEPENDENCE OF NARROW GEOMETRY RATES

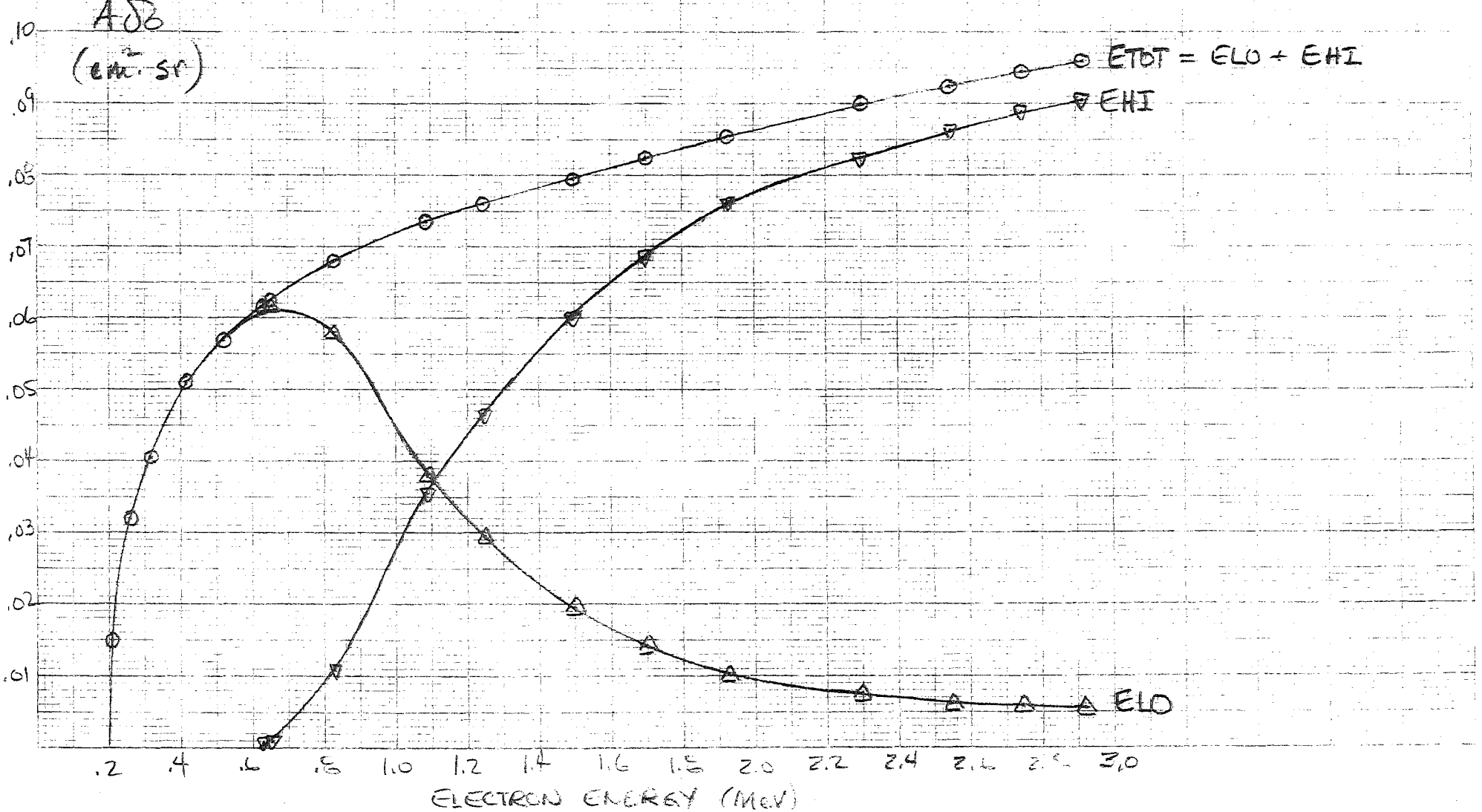

FIGURE IV-7

WIDE GEOMETRY RANGE DISTRIBUTION

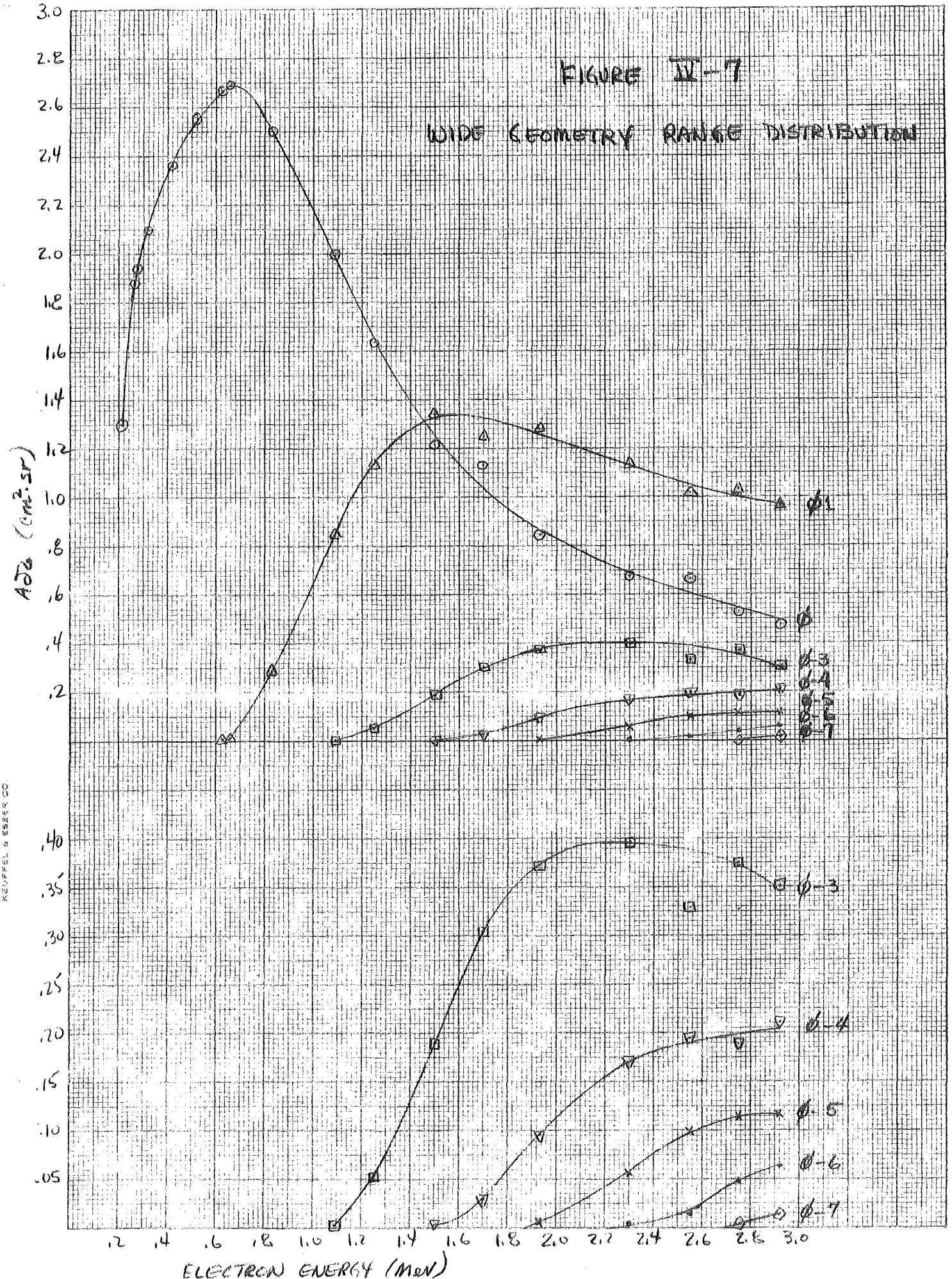

FIGURE IV – 8

ENERGY DEPENDENCE OF NARROW GEOMETRY RANGES

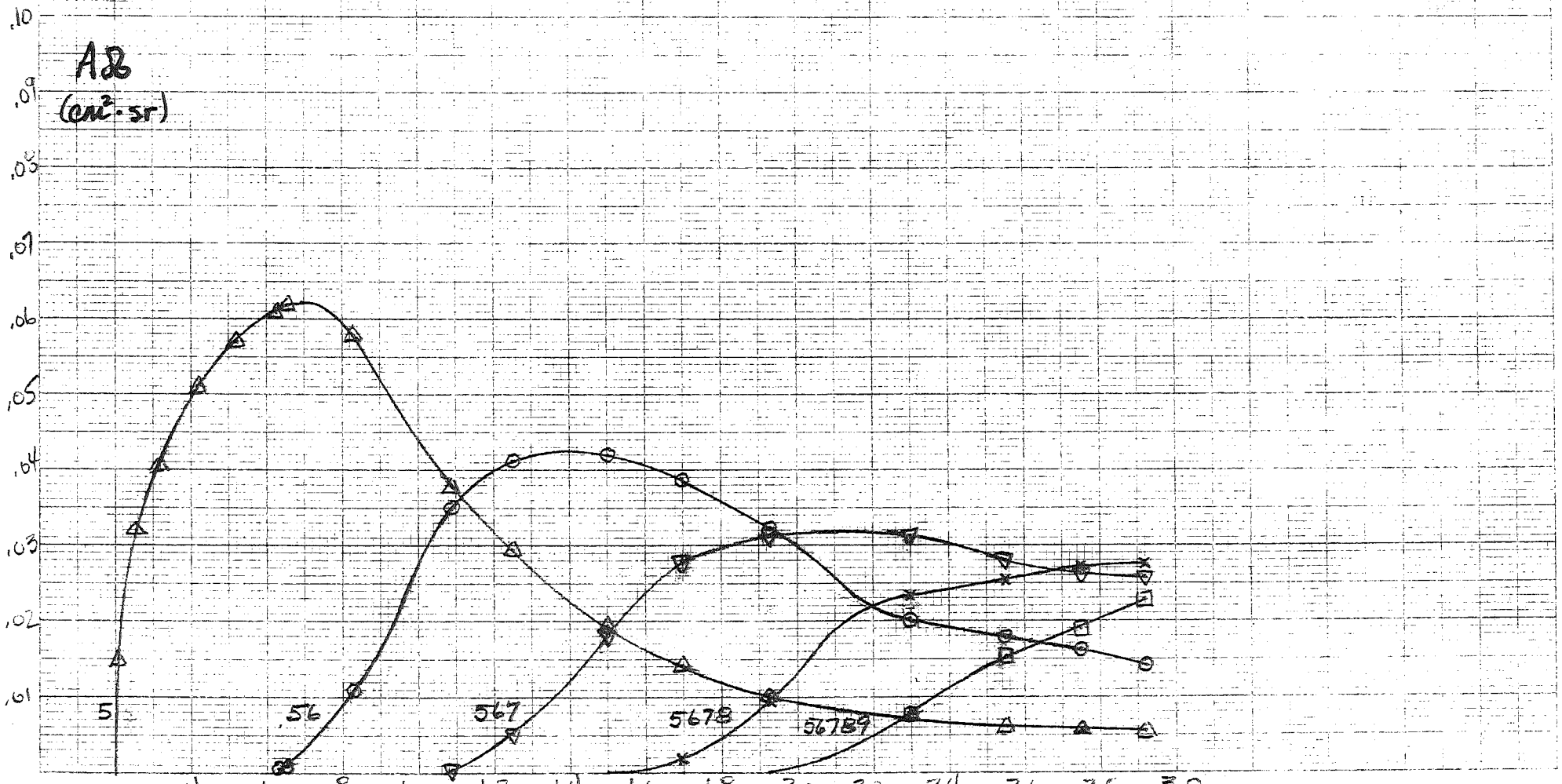

The range distribution of 2.55 MeV electrons shows a systematic deviation from the trend at adjacent energies. The origin of this problem is unknown.

D. Energy Loss Distributions

Figures IV-9 to IV-14 show examples of integrated energy loss distributions for various ranges and energies. The energy index along the abscissa is K ($\sim$ 0.165 MeV scale) or K5 ($\sim$0.041 MeV scale for D5) as defined in Section III-B. The ordinate is the geometry factor in $cm^2 \cdot$ sr (integrated over $\pi/4$).

Note that at all energies that were calibrated, a reasonably well defined total energy peak is visible in at least one range. In general, the deepest range penetrated at any one energy has the best resolution. The location of the total energy peak shifts by $\pm$ .5 channels from range to range because of the compensation method for finite channel width (see Section III-C). This is not a problem if the ranges are treated individually as in Section IV-F.

The wide geometry response shows considerable background at small energy losses in the first few ranges. In particular the 01 range distributions show the effect of electrons scattering from the stack before losing their total energy (note the large space between D1 and D3 in Figure I-1). Thus the predominance of the 01 range at $E > 1.5$ MeV in Figure IV-7 is an indication that lower energy ($\sim$ 1 MeV) measurements in the 01 range will be contaminated considerably by higher energy background if the electron spectrum is sufficiently hard. The low energy background in the D0 range is due mainly to wall-scattered electrons rather than backscattering effects.

The narrow geometry response is much cleaner, although a low energy tail is visible in all ranges at higher incident electron energies. This low energy tail may be due to one or all of the following: 1) Electron leaving the stack by scattering out the interdetector spacing. 2) Electrons reaching D5 by traveling down the outside of the stack. 3) Possible contamination of the beam by low energy electrons scattered within the spectrometer. 4) Compton conversion of bremstrahlung γ-rays produced by the peripheral beam hitting surrounding material. Note that γ-ray induced background due to the Ru-106 source and natural radioactivity has been substracted. Since the narrow geometry mode is of use in flight only for enhanced electron fluxes which typically have soft spectra ($\gamma \gtrsim 3$ for $j(E) \sim E^{-\gamma}$), this background should not be important.

One means of comparing the narrow and wide geometry resolution is to compare the fraction of incident electrons which deposit their total energy. Figure IV-15 shows the geometry factors summed over all ranges for deposition of $\geq 75\%$ of the beam energy. When compared with Figure IV-5 we see that the wide geometry total energy fraction decreases from ~ 0.7 at 0.5 MeV to ~ 0.2 at 3 MeV. The narrow geometry fraction (see Figure IV-6) remains nearly constant at ~ 0.8 until ~ 2.4 MeV, the approximate threshold of PEN events.

Note that the wide geometry total energy geometry factors agree reasonably well with calculated geometry factors for various ranges (Internal report #45). Calculated values include 1.57 $cm^2 \cdot sr$ for D0, 0.75 $cm^2 \cdot sr$ for D013, and 0.39 $cm^2 \cdot sr$ for D0-5. The slight flatening in the wide geometry curve above $\sim$ 2 MeV (Figure IV-15) is possibly due to a significant fraction of electrons reaching the more compact, back part of the stack (range $\geq$ D0-5, Figure I-1).

FIGURE IV-9 D5 GEOMETRY FACTORS

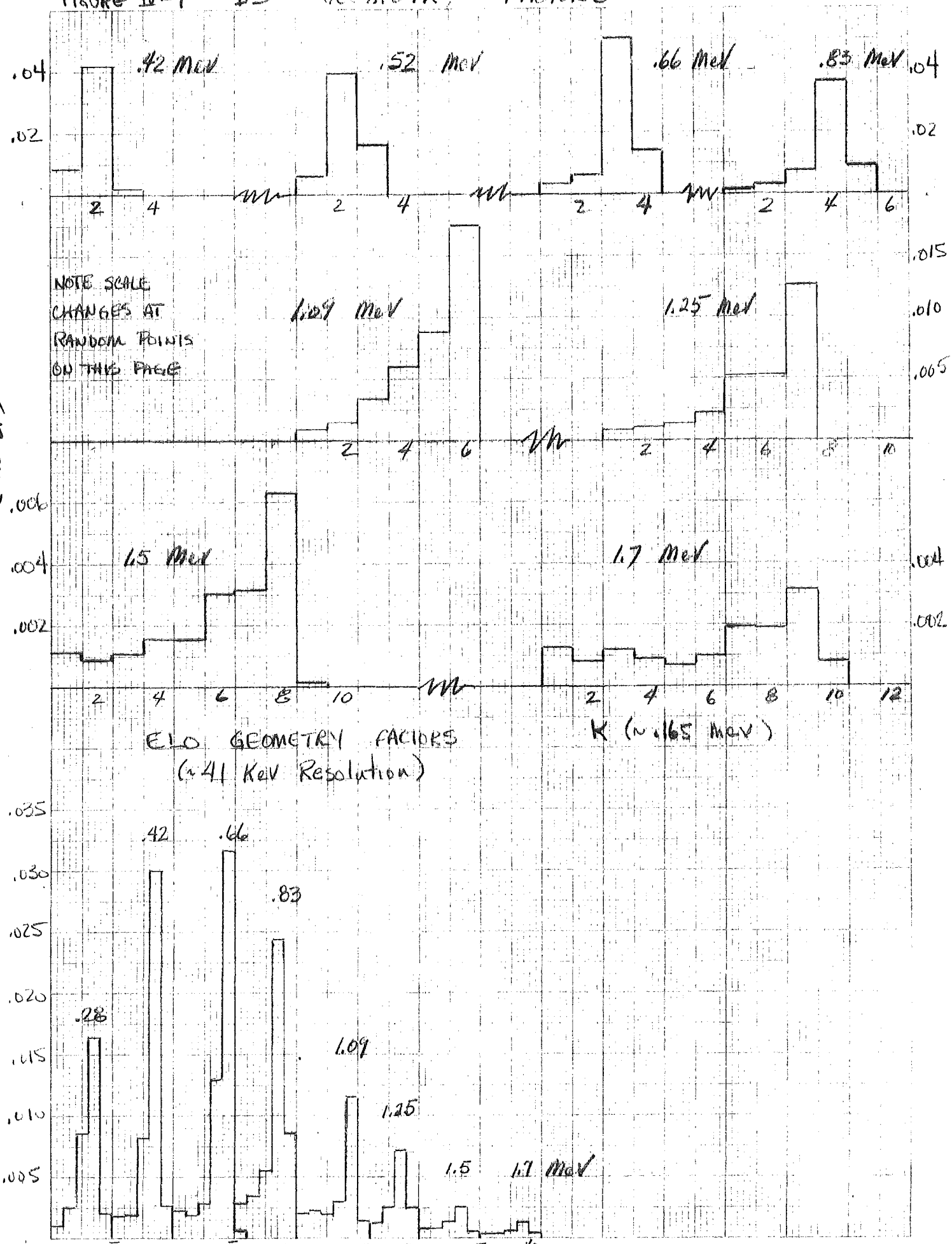

FIGURE IV-10

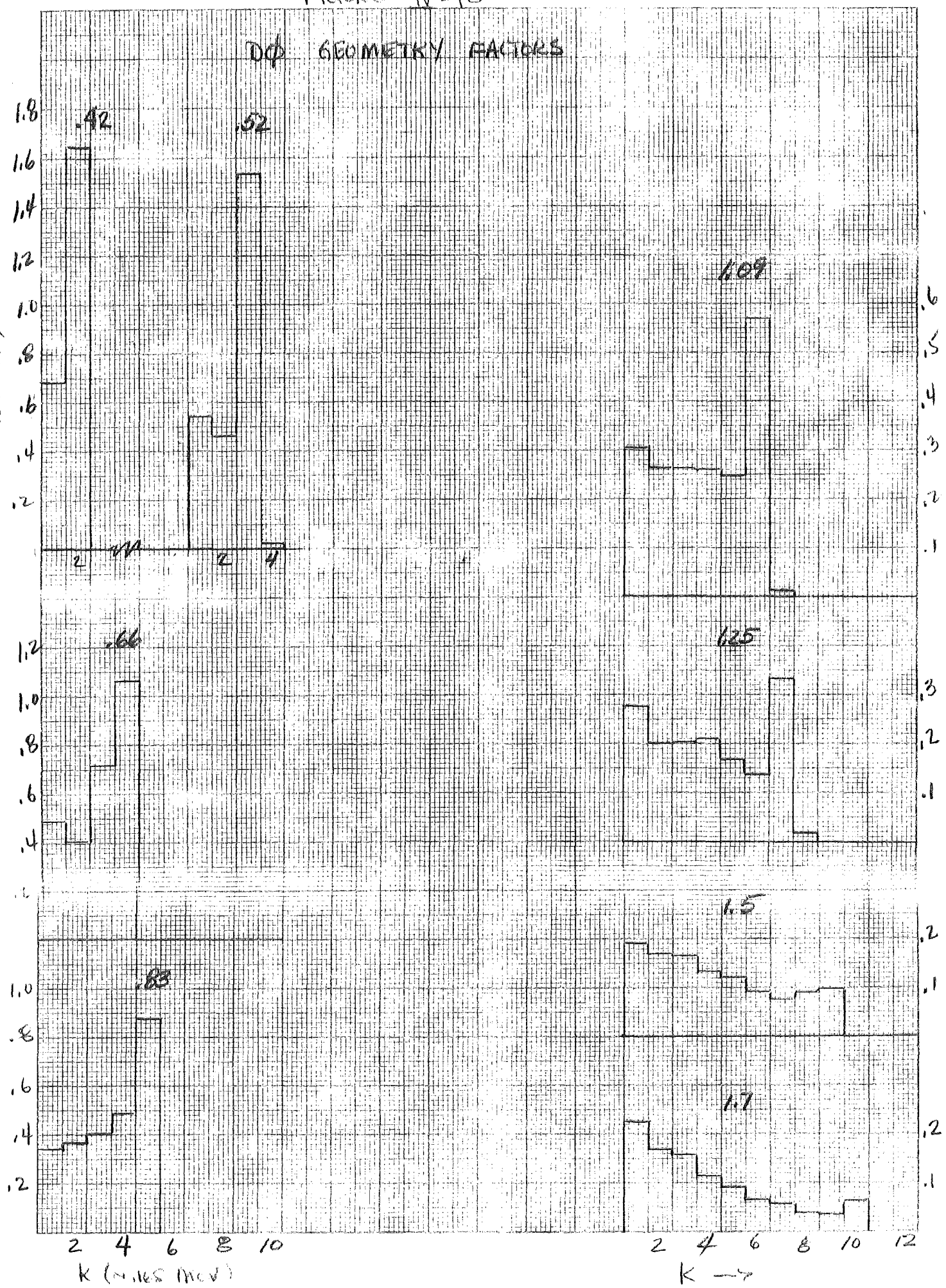

FIGURE IV-11

ENERGY LOSS DISTRIBUTIONS

(.83, 1.09, 1.25 MeV)

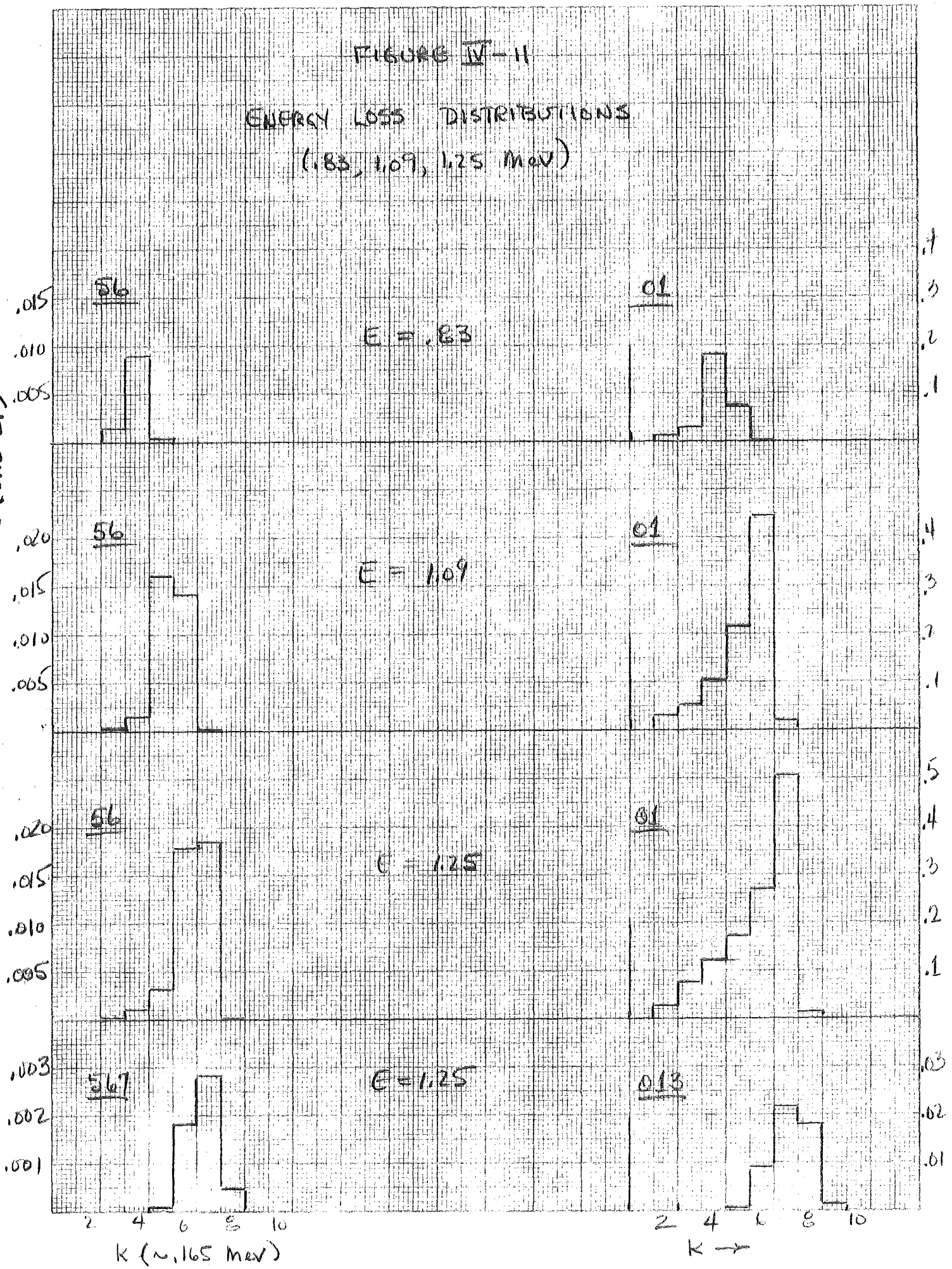

AΔB (cm².sr)

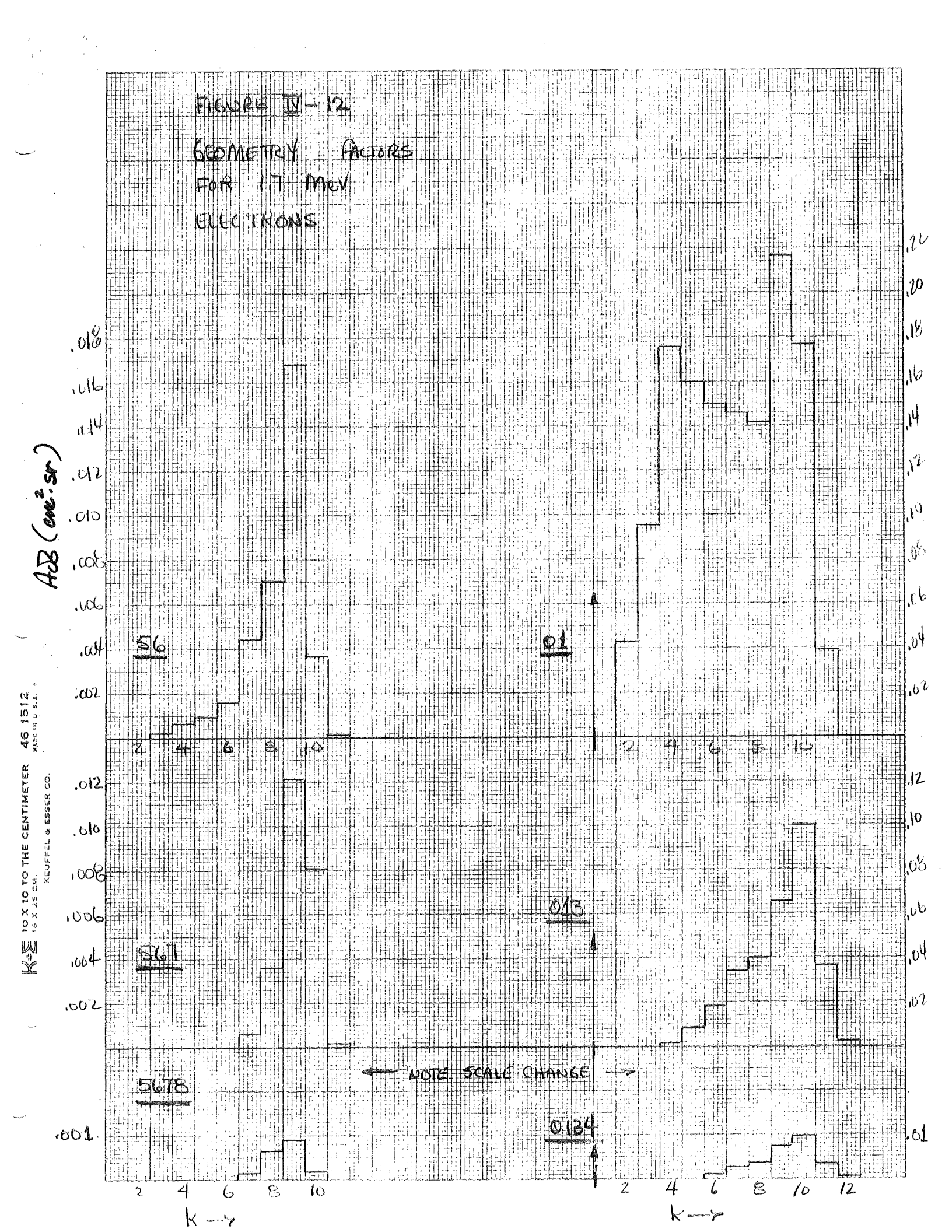
FIGURE IV-12
GEOMETRY FACTORS FOR 17 MeV ELECTRONS
AΩ (cm².sr)
56
01
561
013
5678
0134
NOTE SCALE CHANGE
k →
k →
10 X 10 TO THE CENTIMETER 46 1512
KEUFFEL & ESSER CO.

FIGURE II-13

GEOMETRY FACTORS FOR 2.3 MeV ELECTRONS

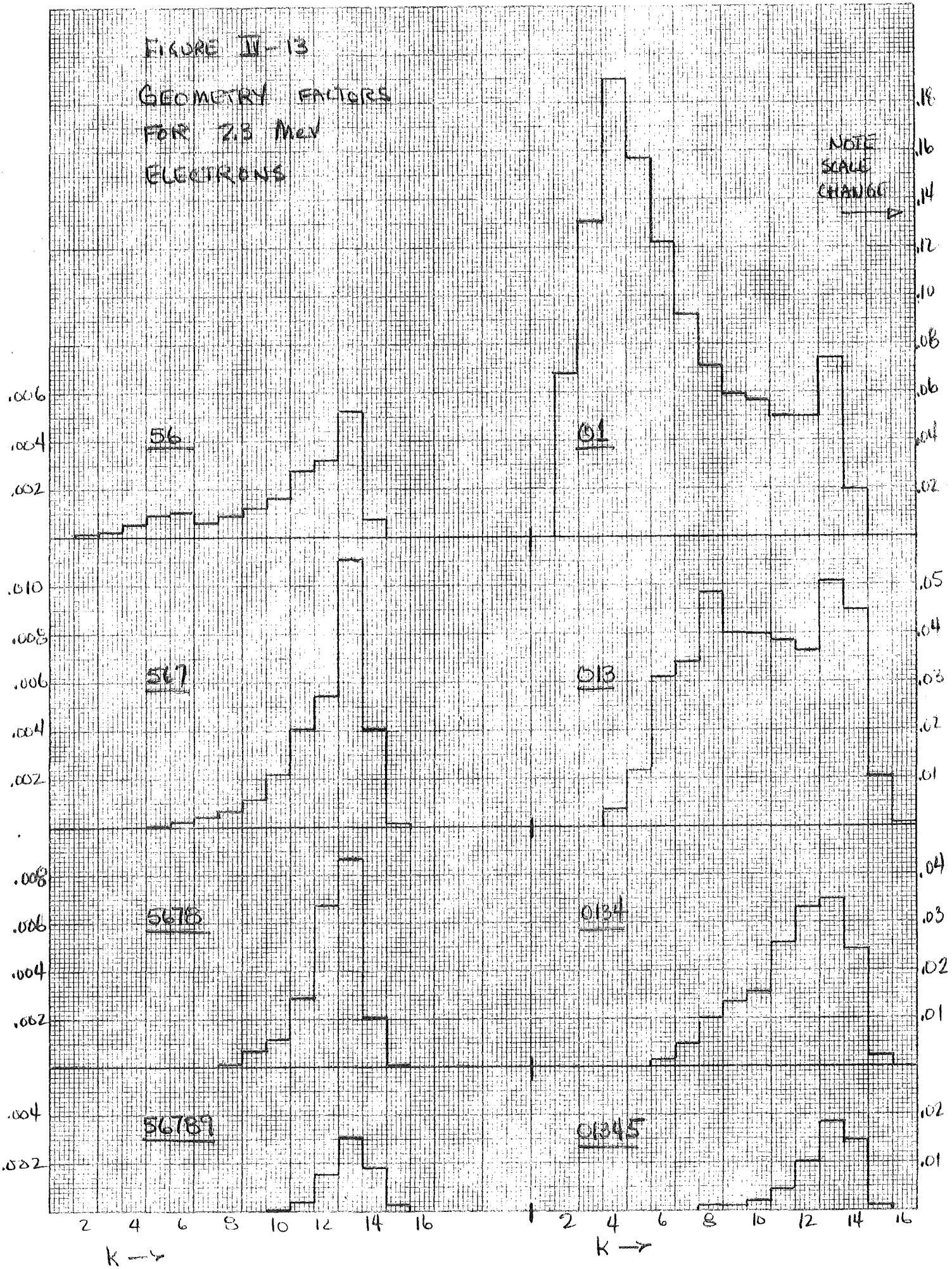

FIGURE IV-14

GEOMETRY FACTORS

FOR 2-9 MeV

ELECTRONS

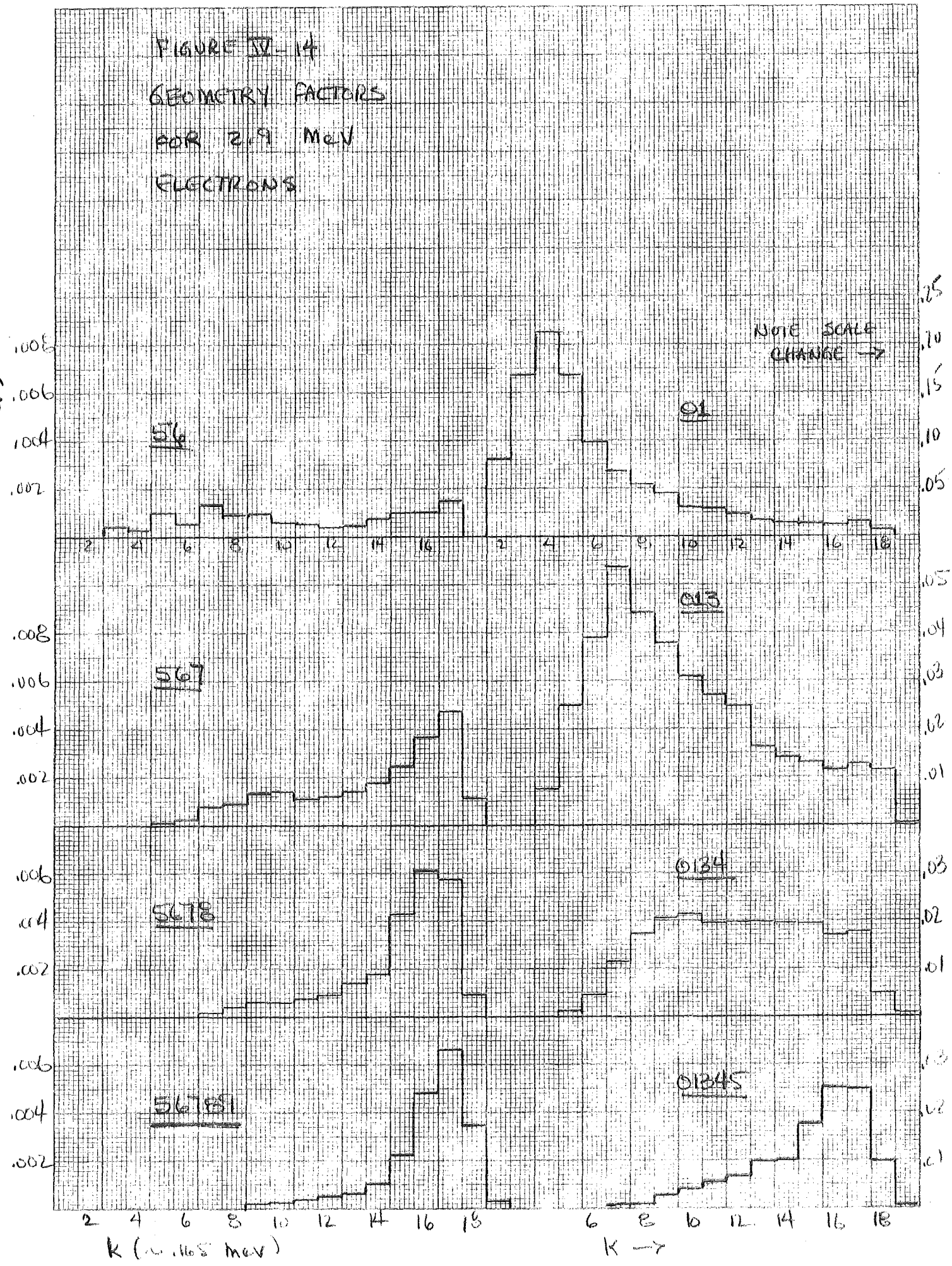

GEOMETRY FACTORS FOR TOTAL ENERGY DEPOSITION

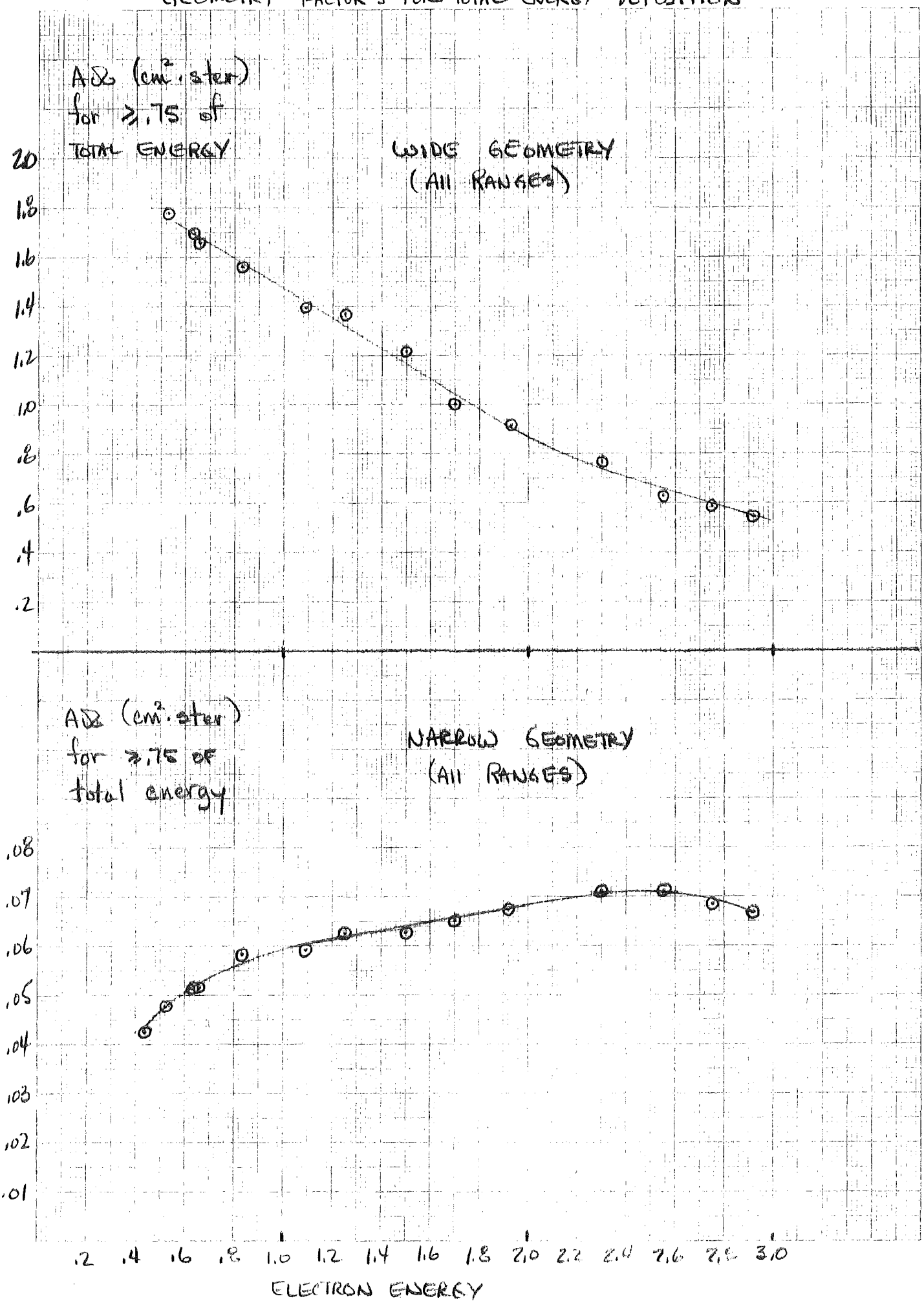

The calculated narrow geometry $A\Omega$ is 0.07 $cm^2 \cdot$ sr, which agrees well with the measured valve at $\gtrsim$ 2 MeV.

E. Thresholds

The low energy D0 response is shown in Figure IV-16. D0 area measurements taken at $\theta = 0^o$ on 2/28/72 were converted to a geometrical factor by normalizing A(.42 MeV) to $A\Omega$(.42 MeV). (To find $A(E,\theta = 0^o)$ multiply $A\Omega$ (E) by 1.30.) The choice of 0.42 MeV is not critical.

Note that the D0 threshold is not sharply defined because of finite detector resolution ($\sigma \sim$ 25 KeV) and energy loss straggling in the window. For soft spectra, electrons down to ~0.14 MeV will contribute significantly to D0 channel 1 events. In the analysis to date it was assumed that for channel 1, $\Delta E = T(2) - T(1) = 0.326 - 0.158 - 0.168$ MeV, and a mean energy E_c and geometrical factor $A\Omega(E_c)$ were defined such that

$$E_c^{-\gamma} \cdot A\Omega(E_c) \cdot \Delta E = \int_0^{0.326} E^{-\gamma} A\Omega(E) dE$$

where γ is the observed spectral index.

Threshold measurements for D0 at $\theta > 0^o$ and for D5 have not yet been analyzed.

F. Wide Geometry Response Matrix

The method of unfolding flight electron spectra that has been pursued so far makes use of a response matrix M(K,J) summarizing the geometrical factors for observed energy losses K due to incident electrons of energy E(J). In this approximation the behavior of all electrons in an energy interval $T(J) \leq E \leq T(J+1)$ is represented by that of an average energy electron with $E = E(J)$, where T(J) is the interval threshold energy.

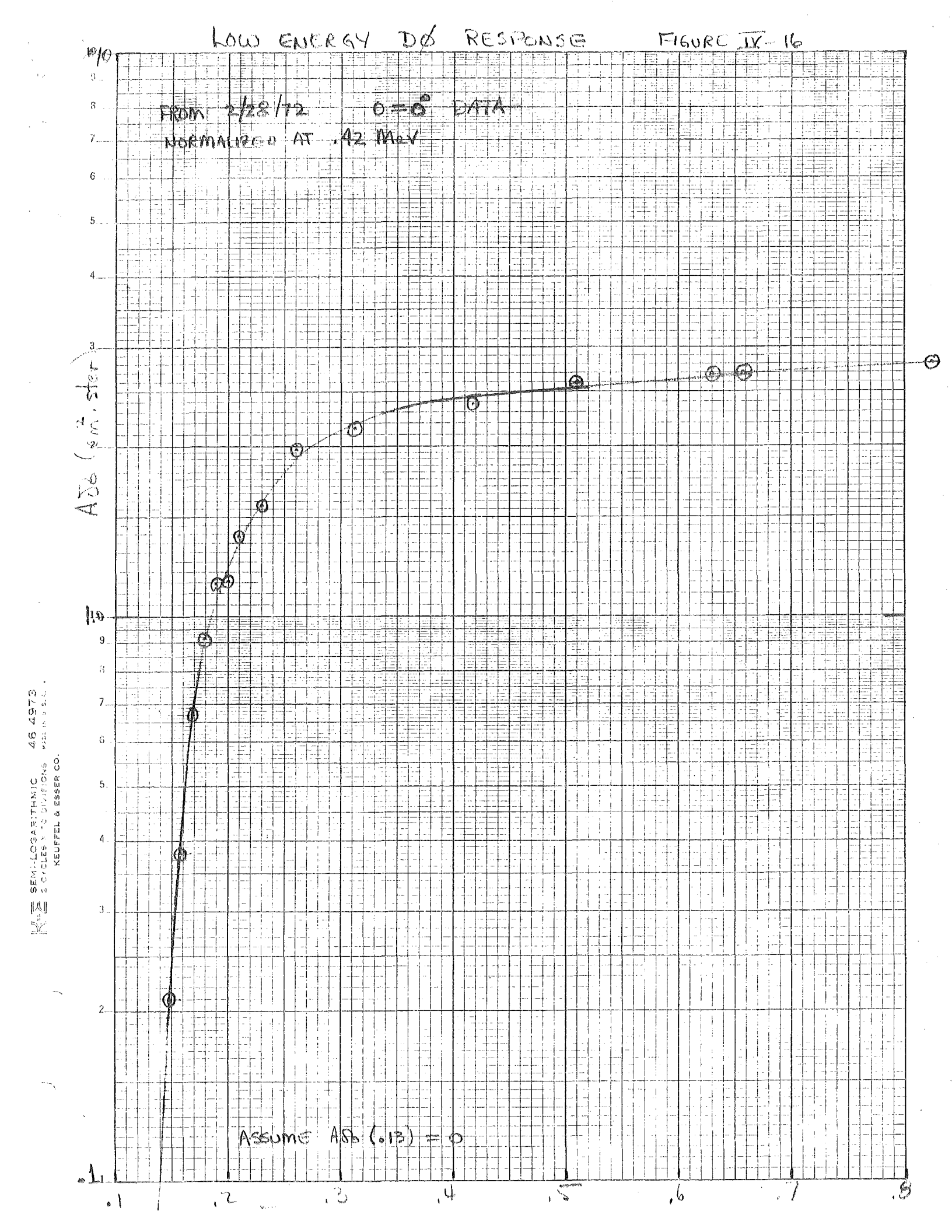
LOW ENERGY DØ RESPONSE
FIGURE IX-16
FROM 2/28/72 θ=0° DATA
NORMALIZED AT .42 MeV
ΔEDØ (cm², ster)
ASSUME ΔEDØ (.13) = 0
SEMI-LOGARITHMIC
46 4973
KEUFFEL & ESSER CO.

Although in principle one should be able to determine the electron flux in each ~ 0.165 MeV interval from ~ 0.16 MeV to the highest energy calibrated (~ 3 MeV), in practice some reduction in the number of energy intervals is necessary in order to achieve stable results. It was also found to be necessary to extrapolate the EIS response above 3 MeV to take into account background at energy losses < 3 MeV due to > 3 MeV electrons.

Ten energy intervals were selected ranging from .16 to 3.76 MeV. The response of each interval was taken to be that of electrons of energy E(J) where

$$[E(J)]^{-2}\,[T(J+1)-T(J)] = \int_{T(J)}^{T(J+1)} E^{-2}EdE \Rightarrow E(J) = [T(J+1)T(J)]^{1/2}$$

The choice of an E^{-2} spectrum is not critical.

Since the energies E(J) do not in general correspond to the calibration energies it was necessary to interpolate the calibration results. The response of an individual channel as a function of the beam energy was found to be well behaved on log-log paper, providing some improvement in consistency over the scatter of the individual calibration points.

In order to incorporate range information the matrix was broken up into 4 levels corresponding to ranges 0,01,013, and 0134 - 013456789, Within a particular range channels were appropriately grouped. An individual level was extended only up to that channel where total energy measurement were still practical (see Figures IV-10 to IV-14). Thus DO data above channel 9 was ignored, for example. At energies $\geq$ ~0.6 MeV matrix elements for a given energy E(J) appear on more than one level. The structure of the matrix should become clear with some study of Table IV-2. The matrix entries are geometrical factors in $cm^2 \cdot ster$.

TABLE IV-2

WIDE GEOMETRY RESPONSE MATRIX

		J ⇒	1	2	3	4	5	6	7	8	9	10
		E(J)	.24	.39	.53	.69	.85	1.09	1.42	1.83	2.40	3.20
		T(J)	.158	.326	.457	.614	.776	.937	1.265	1.598	2.094	2.754
		Δ(J)	.168	.131	.157	.162	.161	.328	.333	.496	.660	.924
	Range	Grouped Channels										
1	0	1	1.750	.930	.726	.589	.498	.413	.334	.275	.222	.177
2		2		1.403	.476	.372	.306	.243	.187	.147	.113	.085
3		3			1.380	.490	.362	.256	.172	.120	.080	.052
4		4				1.213	.417	.264	.155	.096	.056	.032
5		5					.863	.232	.129	.076	.042	.022
6		6-7						.575	.188	.107	.058	.030
7		8-9							.195	.065	.030	.014
8	01	2-4				.089	.190	.201	.251	.321	.390	.441
9		5-6					.146	.535	.357	.301	.263	.240
10		7-8						.128	.550	.243	.156	.098
11		9-11							.081	.374	.141	.084
12		12-15								.012	.127	.044
13	013	4-7							.042	.065	.088	.108
14		8-9							.089	.105	.085	.076
15		10-12								.170	.100	.075
16		13-16									.093	.042
17		17-22										.049
18	0-4+	5-8							.001	.010	.021	.044
19		9-11							.001	.063	.078	.074
20		12-15								.008	.138	.098
21		16-21									.008	.294

IV-G Narrow Geometry Response

The narrow geometry response has not yet been fully analyzed. An approximate method for estimated narrow geometry electron spectra will be presented here. Figure IV-17 shows calculated ELO and EHI rates (sec^{-1}) for electron spectra of the form $j(E) = AE^{-\gamma}$ for A = 1.0.

Thus:

$$ELO(\gamma) = 1.0 \int_0^5 G_{ELO}(E)\, E^{-\gamma}\, dE$$

and

$$EHI(\gamma) = 1.0 \int_0^5 G_{EHI}(E)\, E^{-\gamma}\, dE$$

where the narrow geometry response in Figure IV-6 was extrapolated above E = 3 MeV. The ratio EHI/ELO (curve a) can be used to give γ, and then A can be found from the ELO or EHI curves. The dashed curves show the effect on EHI/ELO for the extreme assumptions that ELO(E) = EHI(E) = 0 for $E \geq 3.0$ MeV (curve b); and ELO(E) = ELO(3), EHI(E) = EHI(3), for $3 \leq E \leq \infty$ (curve c).

Neutral background (see Section V) should be subtracted from ELO and EHI using

$$ELO(\text{Background}) = (.553 \pm .006)\ NEUT$$

$$EHI(\text{Background}) = (.202 \pm .003)\ NEUT$$

These rates were derived from 72:293-7 and 73:016-019 data, which are quiet periods when the ELO, EHI rates are dominated by neutral background. When D7 is off use NEUT $\simeq$ (.0103 $\pm$ .0001) x D8 singles rate.

FIGURE IV-17

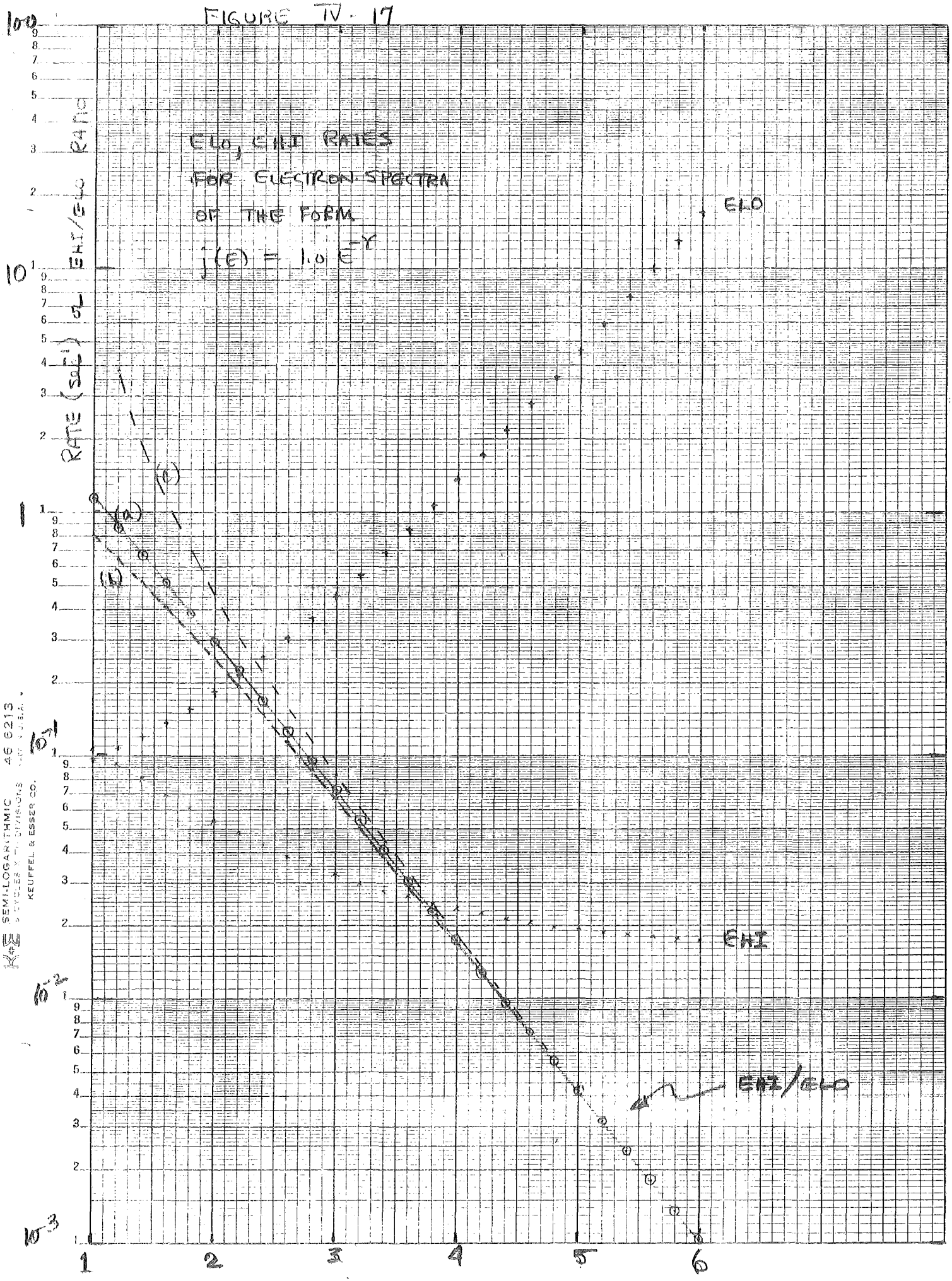

V. FLIGHT DATA

A. Quiet Time Electron Measurements

Table V-I shows typical rates observed during quiet time with the IMP-H EIS, along with the approximate contributions from electrons, neutral particles (mostly γ-rays), and nuclei. Contributions from nuclei (PLO $\lesssim 10^{-3}$) shown for DO* refer to near minimum proton flux levels. Higher proton fluxes (PLO $\gtrsim 10^{-2}$) begin to dominate the DO* count rate. Nuclei do not seriously contaminate electron measurements in ranges ≥ DO1 because they lose more energy than electrons.

TABLE V-I "TYPICAL QUIET-TIME RATES"

NORMALIZED RATE	TOTAL COUNT RATE (sec^{-1})	e^-	γ,n	P,α
DO*	~ .2 - .5	~ .1 - .4	~ .1	~ .01
DO1*	~ .04 - .1	~ .015 - .075	~ .025	$\lesssim$ .005
ELO	~ .05	< .002	~ .05	-
EHI	~ .02	< .0025	~ .02	-
NEUT	~ .09 - .1	-	~ .09 - .1	-

A comparison of the neutral and narrow geometry counting rates (one expects NEUT ≃ ELO + 2·EHI) shows that at quiet time the narrow geometry mode is dominated by γ-ray background. This is demonstrated in Fig. V-1 (Hurford et al., 1973, and 1974) which shows uncorrected energy loss spectra in DO, D5 and D7 for a typical quiet period (72:321-324). Because of its small geometrical factor and the Compton electron background, the narrow geometry mode can be used to analyse

FIGURE V-1

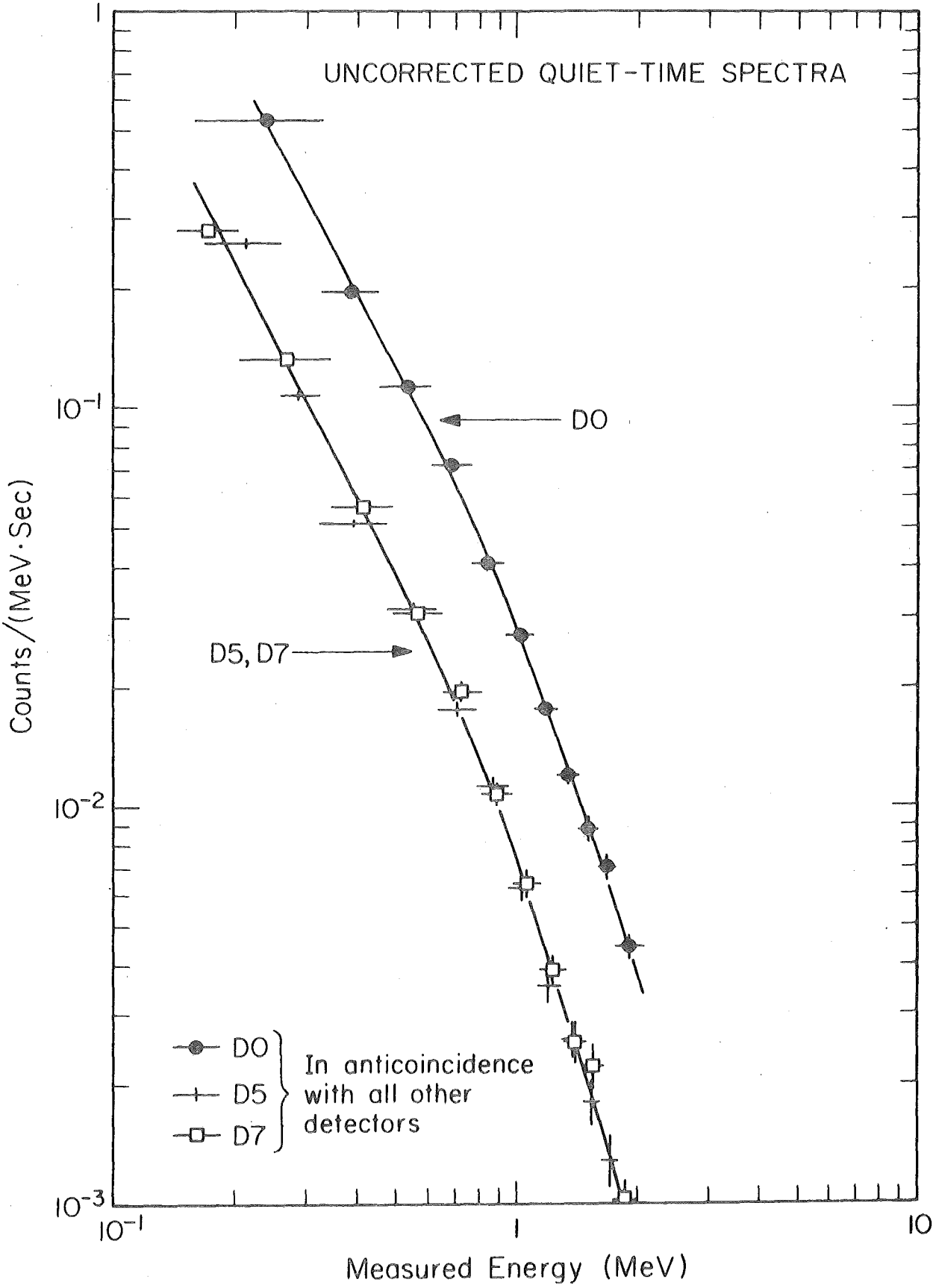
UNCORRECTED QUIET-TIME SPECTRA
D0
D5, D7
D0
D5
D7
In anticoincidence with all other detectors
Counts/(MeV·Sec)
Measured Energy (MeV)
1
10^{-1}
10^{-2}
10^{-3}
10^{-1}
1
10

electrons only during periods of enhanced flux. During solar flares ELO may reach counting rates of 5-50 sec^{-1}, well above the steady γ-ray background level.

Fortunately, quiet time electrons can be measured in the wide geometry mode, once corrections for Compton electrons have been made. The excess counting rate in DO in Figure V-1 is due almost entirely to electrons, with protons contributing < 10% of the DO count rate.

V - B Background Corrections

Two major background contributions must be taken into account before quiet-time electron spectra can be extracted from the wide geometry mode. The first of these, Compton electrons produced in the detector stack by the spacecraft γ-ray background, is discussed in detail in SRL Internal Report #54. The importance of this background was not always recognized in earlier low energy electron measurements.

The second source of background is low energy nuclei which stop in DO, consisting mainly of protons (which deposit 0-13 MeV) and to a much lesser extent alpha particles (0-52 MeV). At the quietest times, nuclei account for less than a few percent of the DO* count rate, although they may account for virtually all of it during periods of solar activity, making electron measurements impossible in DO. Corrections for nuclei are made by measuring their spectrum in D2, which is insensitive to electrons (Lupton and Stone, 1972a).

The general approach is to measure the proton energy loss spectrum in D2, correct for energy loss in the window, and approximate the interplanetary spectrum by a power law $j(E_p) \sim AE_p^B$. This power law fit is then used to predict the proton energy loss spectrum in DO, taking into account the relative narrow and wide geometry

live times and geometrical factors. Table V-2 lists nominal values for relevant parameters that have been used to date.

TABLE V-2 PARAMETERS FOR WIDE GEOMETRY NUCLEI CORRECTION

PARAMETER	NOMINAL VALUE OR DEFINITION
D2 proton $A\Omega$	.2 cm^2 ster
DO proton $A\Omega$	1.8 cm^2 ster
D2 proton threshold (channel 16)	1.213 MeV
DO proton threshold (channel 1)	1.105 MeV
D2 live time	(#PLO EVTS) /CPLO Rate) in sec
DO live time	(#NEUT EVTS) /(NEUT rate) in sec

Note that because the DO proton threshold is lower than that in D2, some extrapolation of the proton spectrum is necessary. In general, the proton rate in DO is ~ 10-15 times that in D2. Thus, uncertainties in this correction are negligible for PLO $\leq 10^{-3}$ (see Table #V-I). At higher PLO rates it has been found that this method predicts up to ~ 20% more protons in DO channels $\gtrsim$10 than are observed, bringing into question the correction for channels < 10. This problem is still under investigation, but some possible contributions to this discrepancy are listed below:

1) The calculated D2 and DO geometry factors may be in error. Perhaps the observed relative rates should be used to define the relative geometry factors, rather than rely on calculated values.

2) Background contributions in D2 (neutrons ?) may cause an overestimate of the proton flux, especially in low D2 channels. This contribution might be estimated by comparing D2 and DO at various proton intensity levels.

3) Variations in counting rate (including anisotropies) over the measurement period lead to incorrect live time estimates, especially if the live times differ significantly for different priority levels.

4) Separate corrections for protons and alpha contributions to DO might have a small effect.

5) If a significant fraction of D7 events ascribed to γ-rays are actually neutron induced, the relative correction factor for D7 and DO (derived from γ-ray calibrations) may be in error. A reduced γ-ray correction at DO channels $\geq$ 10 would reduce but not eliminate the overall discrepancy. The neutron background will be discussed in a later Internal report.

V - C Quiet Time Electron Spectra

The EIS has produced the first low background, high resolution measurements of quiet-time electrons in the .1 - 3 MeV range. Figure V-2 shows the minimum quiet time spectrum observed by the EIS during six quiet time periods analysed from October 72 to January 73. The interpretation of this spectrum is disucssed in Hurford et al (1973, 1974).

Figure V-3 compares the minimum spectrum to one observed during a "quiet-time increase". The 73:069-070 intensity was $\sim$ 3 x higher at energies > .32 MeV. Fluxes $\sim$ 2 x higher than on 73:069-070 were observed on 73:065. It appears to be possible to obtain quiet-time spectra on time scales ranging from $\sim$ 1 day to $\sim$ 1 week, and a systematic investigation of the first $\sim$ 1 1/2 years of IMP-H data is now underway

V - D Flight Data Problems

We mention briefly here a number of additional problems that may be encountered in EIS electron measurements.

1) Disabled detectors - During periods when D7 is disabled the NEUT rate is not available to normalize the neutral background correction. At quiet times a

FIGURE V-2

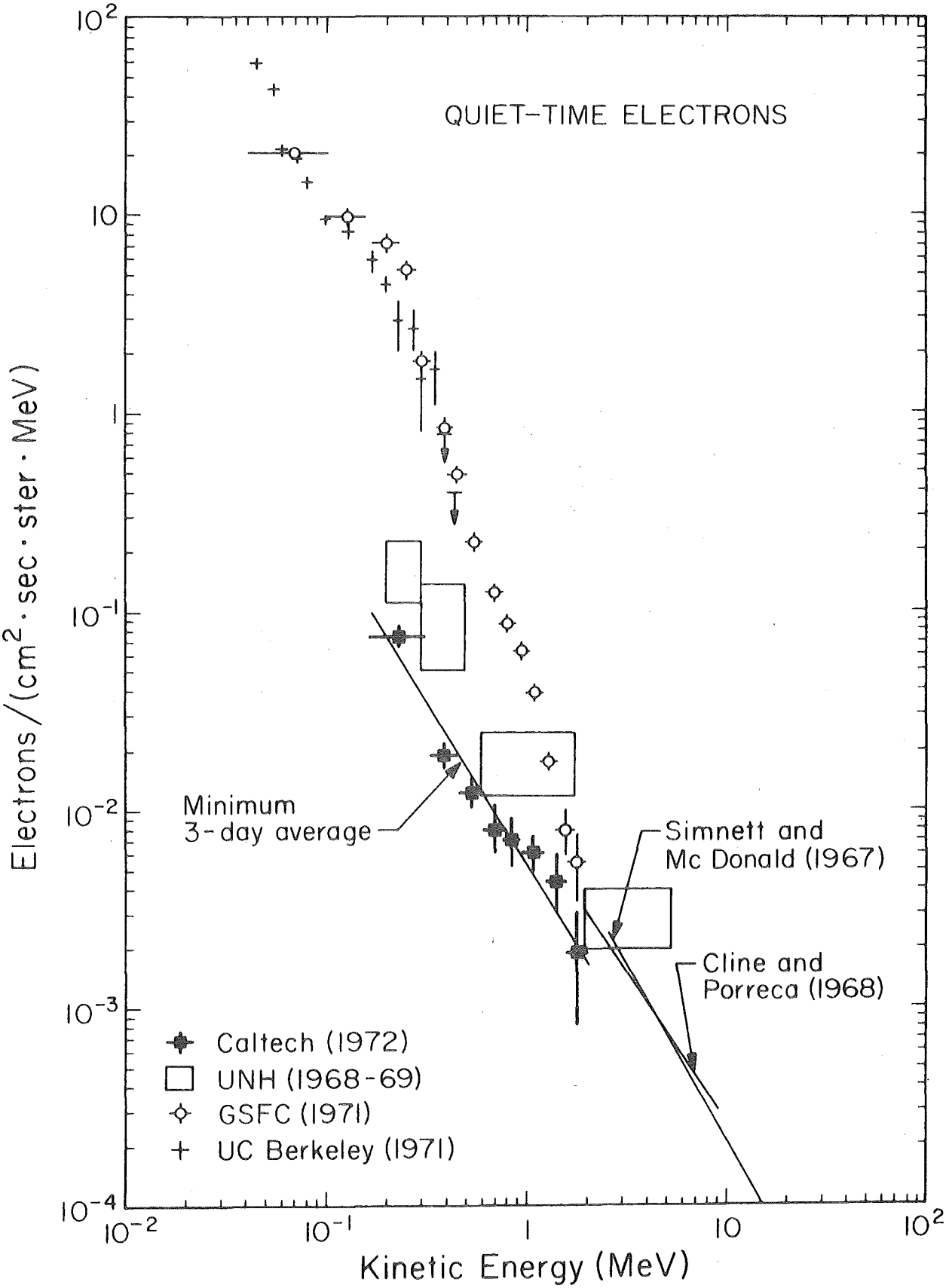
QUIET-TIME ELECTRONS
Electrons / (cm² · sec · ster · MeV)
Kinetic Energy (MeV)
Minimum
3-day average
Simnett and
Mc Donald (1967)
Cline and
Porreca (1968)
Caltech (1972)
UNH (1968-69)
GSFC (1971)
UC Berkeley (1971)

FIGURE V-3

ELECTRON SPECTRA COMPARISON

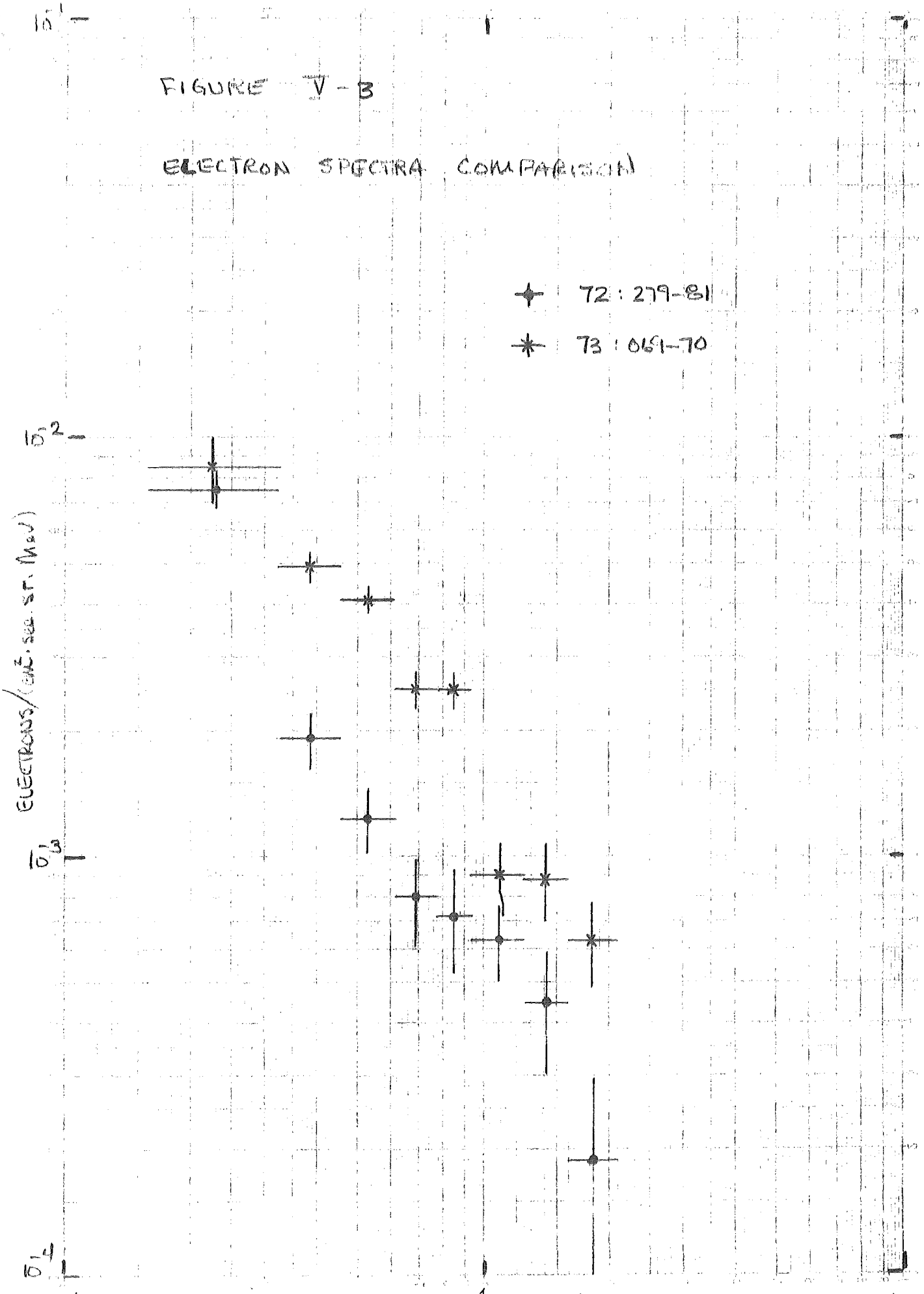

properly normalized ELO, EHI or D8 singles rate may be used for this purpose (see section IV-G). The DO1* rate is the best substitute for computing the priority 2 live time appropriate to a steady event rate.

2) Electron Rate Data - With ELO and EHI dominated by Compton electrons 90% of the time, and DO* dominated by nuclei most of the time, the best available rate for monitoring the quiet time electron intensity is the DO1* rate. Both the Compton electrons and the nuclei contributing to this rate are relatively constant. By subtracting off a background of $\sim .025$ sec^{-1}, time variations in the intensity of electrons $\gtrsim$ 1 MeV are clearly visible.

3) DO channel 1 intensity - At minimum quiet time levels the inferred flux in channel #1 of DO frequently exceeds an extrapolation of the higher energy channels. (see Fig. V-2). Since this problem does not appear in some of the higher intensity spectra studied, it seems unlikely that the DO channel 1 efficiency is seriously in error. Note in Figure V-3 that the .16 - .32 MeV intensities for the two periods are similar, although a significant enhancement is seen at higher energies on 73:069-070. It is likely that DO channel 1 is seeing additional electrons from sources other than those producing the quiet-time interplanetary spectrum at higher energies. Possible other sources include:

a) The high energy tail of the very soft spectrum reported by Lin et al (1972) at E $\lesssim$ 100 KeV. This spectrum was inferred by Lin et al to be of solar origin.

b) Terrestrial electrons arriving at IMP-7 along field lines directly connected to the magnetosphere. Occasional large spikes ($\lesssim$ 3-10 X background) of ~ 10 minute duration are observed on the day side of earth. These fluxes which contribute significantly only in the first channel or so, have ~ 100% anisotropy, directed from earth. Although obvious enhancements of this type

can be eliminated, possible contributions from more frequent, less intense, enhancements of this type would be difficult to detect.

4) Electron Measurements > 2.1 MeV - Although in general consistent results are obtained for electrons < 2.1 MeV, the derived intensities at higher energy generally show an excess over an extrapolation of the lower energy intensities. This effect, which is unlikely to be real, may result from: a) neglect of background due to electrons with E > 3.7 MeV (observed energy losses in wide geometry extend to $\gtrsim$ 5 MeV). b) insufficient subtraction of γ-ray produced background at large energy losses. c) inaccurate extrapolation of the response to E > 2.9 MeV. A finer breakdown of longer range events in D0134 - 9 may help here.

V - E Narrow Geometry Electron Response

The in-flight narrow geometry electron response has not yet been studied in detail. Preliminary comparisons with the wide geometry response during periods of enhanced electron activitity show reasonable agreement. Such comparisons are complicated by live time considerations introduced by the EIS priority system. Note also that cross-talk affects the longer EHI ranges.

VI Future Calibrations

A. Improvements in the Initial IMP-J Calibration

The experience gained during the IMP-H calibrations led to the following improvements in equipment and procedure during the calibrations of the initial IMP-J Stack (identical to IMP-H).

1) The angular range was extended to $0 \lesssim \theta \lesssim 80^0$ through acquisition of a larger bell jar.

2) A direct-readout angular measurement with an accuracy of ~ 1^0 was installed.

3) Considerable attention was devoted to monitoring and controlling

factors affecting the beam intensity and energy.

4) A finer coverage was given to energies in the $.6 \lesssim E \lesssim 1.5$ MeV range, where the range distributions are quite sensitive to the beam energy.

5) More time was devoted to high energies (> 2 MeV) where the range and energy distributions are complex.

6) Low energy points were selected to correspond to the mean response of the first few DO channels.

7) The number of calibration periods was reduced to 2.

B. Recommendations for Future Calibrations

The following suggestions might be considered in planning future calibrations.

1) To reduce systematic effects it is desireable to complete all measurements in a single extended calibration period, with frequent ($\lesssim$ daily) checks at selected energies and angles. Beam energy and intensity calibrations should be performed before and after.

2) The analysis of flight data has shown the need for calibrations at energies > 3 MeV, especially in the wide geometry mode. Figure IV-15 indicates that the geometry factor for depositing the total electron energy is still sizeable above 3 MeV, and the measurement range of the instrument might be extended to ~ 5 MeV. More important is the need for calibrations of the low energy background (< 3 MeV) due to electrons with energies > 3 MeV.

3) A two dimensional analysis procedure might provide improved energy resolution and background rejection. For example, the mean energy loss in the ΔE detector (D0, D5) for multiple detector events is ~ 400 keV. Most Compton electrons lose considerably less than this since they do not penetrate the entire detector. Differences such as this would show up on a 2-D energy plot, although the additional complexity of the analysis would be considerable.

REFERENCES

Lupton, J. E., and E. C. Stone, 1972a, "Measurement of Electron Detection Efficiencies in Solid State Detectors", Nuc. Instrum. and Meth. 98, 189.

Lupton, J. E., and E. C. Stone, 1972b,"Electron Scattering Effects in Typical Cosmic Ray Telescopes, IEEE Trans. NS-19, 562.

Hurford, Mewaldt, Stone, Vogt, "The Energy Spectrum of 0.16 to 2 MeV Electrons During Solar Quiet Times", Ap.J. 192, 541, 1974, and Conference Papers, Thirteenth Intl. Cosmic Ray Conference, Denver 1, 324.

Rossi, B., 1952, "High Energy Particles", Prentice Hall, Englewood Cliffs, N. J.

Bevington, Phillip R., 1969, "Data Reduction and Error Analysis for the Physical Sciences", McGraw-Hill, New York.

Trombka, J. I., 19__, "Least Squares Analysis of γ-ray Pulse Height Spectra" NASA Technical Report #32-373 (from JPL).

Lin, R. P., K. A. Anderson, and T. L. Cline, Phys. Rev. Letters 29, 1035, 1972.

RELEVANT INTERNAL REPORTS

#28	OGO-6 Electron Response	J. L. Lupton
#34	Beta Spectrometer Electronics	S. B. Vidor
#45	Geometrical Factors for IMP-H	S. R. Hartman